PHYSICAL REVIEW B VOLUME 9, NUMBER 11 1 JUNE 1974

Comparison of the Jahn-Teller effect in four triply degenerate states of Mn^{++} in $RbMnF_3$†

Edward I. Solomon* and Donald S. McClure
Department of Chemistry, Princeton University, Princeton, New Jersey 08540
(Received 28 January 1974)

The Jahn-Teller energies and distortions for four excited states of Mn^{++} in $RbMnF_3$ have been obtained. The states are $^4T_1$(I), $^4T_1$(II), $^4T_2$(I), and $^4T_2$(II). An effective force constant and cluster frequency were derived from the data for $^4T_1$(I) and used to find the Jahn-Teller energies for all the states. A semiquantitative treatment of the lattice dynamics of $RbMnF_3$ has enabled us to analyze the phonon sidebands and to describe the coupling of the cluster modes to the lattice. The experimental methods primarily involve the use of uniaxial stress, and the theoretical interpretation involves the calculation of the multiplet splitting, including the reorientation of the exchange field. Both E and T_2 distortions were observed and the Jahn-Teller energies found vary from 58 to 458 cm^{-1}. Even when small, the Jahn-Teller effect has significant spectral consequences. Although we did not use the crystal-field model to analyze the data, we found that it gave a good rationalization of the results.

I. INTRODUCTION

In two previous papers[1,2] an experimental and theoretical study of the Jahn-Teller effect in the $^4T_{1g}$(I) state of $RbMnF_3$ having its spectral origin at 18 221 cm^{-1} was presented. In this paper we extend the analysis to the $^4T_{2g}$(I), $^4T_{2g}$(II), and $^4T_{1g}$(II) states, appearing in the optical-absorption spectrum of $RbMnF_3$ with origins at ~22 000, 27 877, and 32 367 cm^{-1}, respectively (see Fig. 2 of Ref. 3). The two remaining T states lie in the pair-absorption region and were not studied. The four states we studied each have different Jahn-Teller effects, and we believed it would be illuminating to compare these effects in a system where the environment is the same in each. The $RbMnF_3$ crystal has an advantage over a mixed-crystal system in the sense that the positions of the atoms surrounding the Mn^{++} of interest are well known and that other properties of this crystal are very well understood. It was therefore possible to analyze the stress behavior of the spectra and the coupling of the electronic system to lattice vibrations in terms of properties of the pure crystal. The results provide examples of Jahn-Teller effects ranging from weak to strong, relative to the spin-orbit splitting of the T multiplets.

We have modified the analysis of a previous paper[2] so as not to depend on the crystal-field model, and so as to include an effective cluster frequency which takes proper account of the details of the lattice spectrum. The numerical values of the Jahn-Teller energies found are believed to be as accurate as any heretofore obtained. These values lead to a detailed interpretation of many spectral features and allow a great deal of information to be extracted from the optical spectra. The new analysis leads to a critique of the crystal-field model and shows how it can be applied to the Jahn-Teller effect.

After a brief mention of the experimental methods in Sec. II, we outline the theoretical approach in Sec. III. In Sec. IV, the parameters of the lattice cluster model are obtained. The lattice dynamics of $RbMnF_3$ and the phonon sidebands of the four transitions are considered in Sec. V. We give the experimental results and analysis for the $^4T_1$(II), and $^4T_2$(II) states in Secs. VI and VII. We obtained very little information from the broad spectrum of the $^4T_2$(I) state, but use the results from the other states to give a plausible explanation of it in Sec. VIII. Then in Sec. IX, the Jahn-Teller effects as measured by several methods for the four states are compared and discussed, and Sec. X is the critique of the crystal-field model.

II. EXPERIMENTAL METHODS

The experimental methods used were described in Ref. 1. We would like to add here some remarks about the $RbMnF_3$ samples used.

We have used samples from several sources with varying amounts of impurities and internal strains. The best material was that grown by Guggenheim of Bell Laboratories.[4] We find the energies of the transitions to vary from sample to sample. There is about a 15-cm^{-1} range for $^4T_1$(I) and $^4T_1$(II), and a 5-cm^{-1} range for $^4T_2$(II). All the numbers we give are adjusted to those of the samples having the highest purity. We also found several samples which appeared to be single crystals but gave very diffuse Laue patterns. These did not show the spin reorientation stress effects that were dominant in most of our samples.

Also for some transitions when the crystal is under stress there is only partial polarization even at high-stress values. These effects are real, as we have looked at other spectral regions while taking the data and find the polarizations there to be complete.

III. HAMILTONIAN AND WAVE FUNCTIONS

Before proceeding with the actual calculations and interpretation of the data, we will outline the theoretical background. As we will be interested in the ${}^6A_{1g} \rightarrow {}^4\Gamma_g$ ($\Gamma_g = T_{2g}$ or T_{1g}) transitions, we give in Table I the d^5 orbital-triplet (X, Y, Z for T_1 or ξ, η, ζ for T_2) spin-quartet many-electron wave functions for strong-field terms.

Implicit in each of the three orbital partners for each strong-field term are four spin projections ($M_s = \frac{3}{2}, \frac{1}{2}, -\frac{1}{2}$, and $-\frac{3}{2}$), making the total degeneracy 12.

In order to obtain wave functions corresponding to the observed transitions, we must now allow for configurational interaction between strong-field terms of the same symmetry. This is done by diagonalizing the Tanabe and Sugano[5] d^5 ${}^4T_1$ and ${}^4T_2$ matrices, using $B = 840$, $C = 3080$, and $Dq = 780$ cm^{-1}, which were found[6] to fit the 77 °K spectrum. From these solutions we find the coefficients of the configurationally mixed crystal-field wave function

$$\Psi({}^4\Gamma_g,\ i) = \alpha\,|{}^4\Gamma_g,\ t^4e\rangle + \beta\,|{}^4\Gamma_g,\ t^3e^2\rangle + \gamma\,|{}^4\Gamma_g,\ t^2e^3\rangle,$$

where i = I, II, or III. These coefficients are listed in Table II.

Assuming that we have the correct octahedral wave functions, we now write the complete vibronic

TABLE I. Strong-field d^5 orbital-triplet spin-quartet real many-electron wave functions.

$|{}^4T_1,\ t_2^4e,\ X\rangle = \frac{1}{2}|\xi\ \bar{\xi}\ \eta\ \zeta\ \theta\rangle - \frac{1}{2}(3)^{1/2}|\xi\ \bar{\xi}\ \eta\ \zeta\ \epsilon\rangle$

$|{}^4T_1,\ t_2^4e,\ Y\rangle = -\frac{1}{2}|\xi\ \eta\ \bar{\eta}\ \zeta\ \theta\rangle - \frac{1}{2}(3)^{1/2}|\xi\ \eta\ \bar{\eta}\ \zeta\ \epsilon\rangle$

$|{}^4T_1,\ t_2^4e,\ Z\rangle = -|\xi\ \eta\ \zeta\ \bar{\zeta}\ \theta\rangle$

$|{}^4T_1,\ t_2^3e^2,\ X\rangle = (2)^{-1/2}\{|\xi\ \zeta\ \bar{\zeta}\ \theta\ \epsilon\rangle + |\zeta\ \eta\ \bar{\eta}\ \theta\ \epsilon\rangle\}$

$|{}^4T_1,\ t_2^3e^2,\ Y\rangle = (2)^{-1/2}\{|\eta\ \zeta\ \bar{\zeta}\ \theta\ \epsilon\rangle + |\xi\ \bar{\xi}\ \eta\ \theta\ \epsilon\rangle\}$

$|{}^4T_1,\ t_2^3e^2,\ Z\rangle = (2)^{-1/2}\{|\xi\ \bar{\xi}\ \zeta\ \theta\ \epsilon\rangle + |\eta\ \bar{\eta}\ \zeta\ \theta\ \epsilon\rangle\}$

$|{}^4T_1,\ t_2^2e^3,\ X\rangle = -\frac{1}{2}|\zeta\ \eta\ \theta\ \epsilon\ \bar{\epsilon}\rangle + \frac{1}{2}(3)^{1/2}|\zeta\ \eta\ \theta\ \bar{\theta}\ \epsilon\rangle$

$|{}^4T_1,\ t_2^2e^3,\ Y\rangle = -\frac{1}{2}|\xi\ \zeta\ \theta\ \epsilon\ \bar{\epsilon}\rangle - \frac{1}{2}(3)^{1/2}|\xi\ \zeta\ \theta\ \bar{\theta}\ \epsilon\rangle$

$|{}^4T_1,\ t_2^2e^3,\ Z\rangle = |\eta\ \xi\ \theta\ \epsilon\ \bar{\epsilon}\rangle$

$|{}^4T_2,\ t_2^4e,\ \xi\rangle = \frac{1}{2}(3)^{1/2}|\xi\ \bar{\xi}\ \eta\ \zeta\ \theta\rangle + \frac{1}{2}|\xi\ \bar{\xi}\ \eta\ \zeta\ \epsilon\rangle$

$|{}^4T_2,\ t_2^4e,\ \eta\rangle = \frac{1}{2}(3)^{1/2}|\xi\ \eta\ \bar{\eta}\ \zeta\ \theta\rangle - \frac{1}{2}|\xi\ \eta\ \bar{\eta}\ \zeta\ \epsilon\rangle$

$|{}^4T_2,\ t_2^4e,\ \zeta\rangle = -|\xi\ \eta\ \zeta\ \bar{\zeta}\ \epsilon\rangle$

$|{}^4T_2,\ t_2^3e^2,\ \xi\rangle = (2)^{-1/2}\{|\xi\ \eta\ \bar{\eta}\ \theta\ \epsilon\rangle - |\xi\ \zeta\ \bar{\zeta}\ \theta\ \epsilon\rangle\}$

$|{}^4T_2,\ t_2^3e^2,\ \eta\rangle = (2)^{-1/2}\{|\eta\ \zeta\ \bar{\zeta}\ \theta\ \epsilon\rangle - |\xi\ \bar{\xi}\ \eta\ \theta\ \epsilon\rangle\}$

$|{}^4T_2,\ t_2^3e^2,\ \zeta\rangle = (2)^{-1/2}\{|\xi\ \bar{\xi}\ \zeta\ \theta\ \epsilon\rangle - |\eta\ \bar{\eta}\ \zeta\ \theta\ \epsilon\rangle\}$

$|{}^4T_2,\ t_2^2e^3,\ \xi\rangle = -\frac{1}{2}(3)^{1/2}|\zeta\ \eta\ \theta\ \epsilon\ \bar{\epsilon}\rangle - \frac{1}{2}|\zeta\ \eta\ \theta\ \bar{\theta}\ \epsilon\rangle$

$|{}^4T_2,\ t_2^2e^3,\ \eta\rangle = +\frac{1}{2}(3)^{1/2}|\xi\ \zeta\ \theta\ \epsilon\ \bar{\epsilon}\rangle - \frac{1}{2}|\xi\ \zeta\ \theta\ \bar{\theta}\ \epsilon\rangle$

$|{}^4T_2,\ t_2^2e^3,\ \zeta\rangle = +|\eta\ \xi\ \theta\ \bar{\theta}\ \epsilon\rangle$

TABLE II. Coefficients of configuration components in the strong-field wave functions.

	α (t^4e)	β (t^3e^2)	γ (t^2e^3)	$\alpha^2 - \gamma^2$
${}^4T_{1g}$(I)	0.977 19	0.151 74	−0.148 54	0.93
${}^4T_{1g}$(II)	0.034 18	0.578 02	0.815 31	−0.66
${}^4T_{2g}$(I)	0.794 95	−0.517 24	−0.317 04	0.53
${}^4T_{2g}$(II)	−0.509 99	−0.852 79	0.112 52	0.25

effective Hamiltonian which operates on a given orbtial triplet

$$\Psi = \begin{bmatrix} X \\ Y \\ Z \end{bmatrix} \text{ for } T_1 \text{ or } \begin{bmatrix} \xi \\ \eta \\ \zeta \end{bmatrix} \text{ for } T_2; \qquad (3.1)$$

$$\mathcal{H} = \mathcal{H}_{\text{vib}} + \mathcal{H}_{\text{so}} + \mathcal{H}_{\text{ex}} + \mathcal{H}_{\text{stress}}.$$

The terms are now discussed in order.

A. Terms relating to Eq. (3.1a)

$$\mathcal{H}_{\text{vib}} = \frac{1}{2}\sum^{r} \frac{P_r^2 + \mu_r^2\omega_r^2 Q_r^2}{\mu_r} + V_{A_{1g}}\begin{bmatrix} Q_A & 0 & 0 \\ 0 & Q_A & 0 \\ 0 & 0 & Q_A \end{bmatrix}$$
$$+ V_{E_g}\begin{bmatrix} -\frac{1}{2}\sqrt{3}\,Q_\epsilon + \frac{1}{2}Q_\theta & 0 & 0 \\ 0 & \frac{1}{2}\sqrt{3}\,Q_\epsilon + \frac{1}{2}Q_\theta & 0 \\ 0 & 0 & -Q_\theta \end{bmatrix}$$
$$+ V_{T_{2g}}\begin{bmatrix} 0 & Q_\zeta & Q_\eta \\ Q_\zeta & 0 & Q_\xi \\ Q_\eta & Q_\xi & 0 \end{bmatrix}. \qquad (3.1a)$$

$\mathcal{H}_{\text{vib}}$ serves two purposes. The $K_r (= \mu_r\omega_r^2)$ determines the vibrational frequencies, and the ratio of V_r/K_r determines the Jahn-Teller coupling, which produces displacement of the near neighbors and is responsible for the strength of various vibrations in the sidebands. The Q_r describing allowed displacements of nearest neighbors for a T state in a cubic environment are given in terms of the MnF_6^{-4} cluster by[7]

$$\begin{aligned} Q_A &= (1/\sqrt{6})[(X_1 - X_4) + (Y_2 - Y_5) + (Z_3 - Z_6)], \\ Q_\theta &= (1/\sqrt{12})[2(Z_3 - Z_6) - (X_1 - X_4) - Y_2 - Y_5)], \\ Q_\epsilon &= (1/\sqrt{4})[(X_1 - X_4) - (Y_2 - Y_5)], \\ Q_\xi &= (1/\sqrt{4})[(Z_2 - Z_5) + (Y_3 - Y_6)], \\ Q_\eta &= (1/\sqrt{4})[(X_3 - X_6) + (Z_1 - Z_4)], \\ Q_\zeta &= (1/\sqrt{4})[(Y_1 - Y_4) + (X_2 - X_5)], \end{aligned} \qquad (3.2)$$

and are illustrated in Ref. 8.

The excitation is treated as if it were immobilized in the crystal since the exciton bandwidth ap-

pears to be practically zero. Therefore, the interesting even-parity vibrations belong to the subset of lattice modes for which the excitation is fixed on one Mn atom. This fact allows us to classify the crystal modes in terms of the A_{1g}, E_g, and T_{2g} representations of the cubic point group. The Q_γ expressed in terms of the plane-wave normal modes, $k_{q,\lambda}$, of the crystal are (the notation is explained in Ref. 2 and we use the normalization conditions of Peierls[9])

$$
\begin{aligned}
Q_A &= 2i\frac{1}{\sqrt{6}}\sum_{\vec{q},\lambda}[\epsilon^{F_x}_{\vec{q},\lambda,x}\sin(\tfrac{1}{2}q_x a)+\epsilon^{F_y}_{\vec{q},\lambda,y}\sin(\tfrac{1}{2}q_y a)\\
&\quad+\epsilon^{F_z}_{\vec{q},\lambda,z}\sin(\tfrac{1}{2}q_z a)]\,k_{q,\lambda},\\
Q_\theta &= 2i\frac{1}{\sqrt{12}}\sum_{\vec{q},\lambda}[2\epsilon^{F_z}_{\vec{q},\lambda,z}\sin(\tfrac{1}{2}q_z a)-\epsilon^{F_y}_{\vec{q},\lambda,y}\sin(\tfrac{1}{2}q_y a)\\
&\quad-\epsilon^{F_x}_{\vec{q},\lambda,x}\sin(\tfrac{1}{2}q_x a)]\,k_{q,\lambda},\\
Q_\epsilon &= 2i\frac{1}{\sqrt{4}}\sum_{\vec{q},\lambda}[\epsilon^{F_x}_{\vec{q},\lambda,x}\sin(\tfrac{1}{2}q_x a)\\
&\quad-\epsilon^{F_y}_{\vec{q},\lambda,y}\sin(\tfrac{1}{2}q_y a)]k_{q,\lambda},\\
Q_\zeta &= 2i\frac{1}{\sqrt{4}}\sum_{\vec{q},\lambda}[\epsilon^{F_y}_{\vec{q},\lambda,z}\sin(\tfrac{1}{2}q_y a)\\
&\quad+\epsilon^{F_z}_{\vec{q},\lambda,y}\sin(\tfrac{1}{2}q_z a)]\,k_{q,\lambda},\\
Q_\eta &= 2i\frac{1}{\sqrt{4}}\sum_{\vec{q},\lambda}[\epsilon^{F_z}_{\vec{q},\lambda,x}\sin(\tfrac{1}{2}q_z a)\\
&\quad+\epsilon^{F_x}_{\vec{q},\lambda,z}\sin(\tfrac{1}{2}q_x a)]\,k_{q,\lambda},\\
Q_\xi &= 2i\frac{1}{\sqrt{4}}\sum_{\vec{q},\lambda}[\epsilon^{F_x}_{\vec{q},\lambda,y}\sin(\tfrac{1}{2}q_x a)\\
&\quad+\epsilon^{F_y}_{\vec{q},\lambda,x}\sin(\tfrac{1}{2}q_y a)]\,k_{q,\lambda}.
\end{aligned}
\tag{3.3}
$$

The $k_{\vec{q},\lambda}$ diagonalize a vibrational Hamiltonian as Eq. (3.1a) having the associated frequency $\omega_{\vec{q},\lambda}$, a linear coupling coefficient $V^\gamma_{\vec{q},\lambda}$, and a mass equal to that of the crystal $N\sum_s M_s$. Extended cluster vibrations involving many neighbors could be significant, but see Ref. 10.

The totally symmetric A_{1g} mode is seen from Eq. (3.1a) to displace all three electronic partners equally in Q_A space and it therefore leads to a distortion with no electronic mixing. Such a distortion has no effect on energies within the multiplet but shifts the excited state geometry relative to the ground state and thus contributes to the vibrational progression. The distortion and its associated energy are given by

$$d_A = V_A/K_A, \tag{3.4a}$$

$$E_A = V_A^2/2K_A \tag{3.4b}$$

(where V is a linear coupling constant and K is a harmonic force constant).

The E_g force is also seen to be diagonal in the electronic partners but with each partner forced into a different configuration in Q_θ, Q_ϵ space and therefore electronically pure, but spatially separated. The displacement along a θ-type direction and the corresponding energy are

$$d_E = V_E/K_E, \tag{3.5a}$$

$$E_E = V_E^2/2K_E. \tag{3.5b}$$

The relative spatial separation of the partners has the effect of reducing matrix elements between different partners by the overlap of the zeroth vibrational levels of the displaced-harmonic-oscillator wave functions. The Ham reduction factor[11] is

$$R_E = e^{-3E_E/2\hbar\omega_E}. \tag{3.5c}$$

Matrix elements diagonal within an X, Y, Z (ξ, η, ζ) basis will not be reduced. We note that we obtain from experiment a fairly accurate value of R_E and not the Jahn-Teller energy E_E directly. To get the latter, we need to know the vibrational frequency of the E_g mode in Eq. (3.5c). Since we are not dealing with an impurity which changes the local force constants enough to cause local modes, we must express R_E in terms of the propagating modes of the pure lattice. Thus the reduction factor becomes

$$R_E = \exp\left(-\frac{3}{2}\sum_{\vec{q},\lambda}\frac{(V^E_{\vec{q},\lambda})^2}{(2K_{\vec{q},\lambda}\hbar\omega_{\vec{q},\lambda})}\right),$$

where $K_{\vec{q},\lambda}$ is the force constant of the $\vec{q},\lambda$ mode (see, for example, Ref. 11). Thus, in order to obtain an estimate of E_E we must use an effective $\bar{\omega}_E$ which accounts for coupling to the phonon continuum. The lower frequencies have a larger reduction factor because of the $1/\omega$ dependence in the exponent. Within the cluster approximation there will be an associated effective force constant, $\bar{K}_E = \mu_E\bar{\omega}_E^2$, where μ_E is the mass of the fluorine and $\bar{\omega}_E$ is an effective frequency. This frequency will be somewhat less than the maximum value of 470 cm^{-1} assumed in Ref. 2 (see Sec. IV).

The T_{2g} forces cannot be diagonalized within the electronic partners, but instead lead to the distortions

$$(2V_T/3K_T)(Q_\xi, Q_\eta, Q_\zeta) \tag{3.6a}$$

along four equivalent [111] directions. The Jahn-Teller energy is

$$E_T = 2V_T^2/3K_T. \tag{3.6b}$$

This leaves a complicated vibronic problem to be solved numerically. The results[12] of such a solution are given in Sec. VI. Ham[11] gives approximate quenching factors for the response to T_{2g} distortion. The trigonal splitting will be only partially quenched by a factor of the form $(\frac{2}{3}+\frac{1}{3}e^{-(9/4)E_T/\hbar\omega_T})$. This reflects the fact that the T_{2g} electronic matrix cannot be completely diagonalized in any one distortion direction. The nontrigonal terms will be

strongly quenched by a factor R_T as $e^{-(9/4)E_T/\hbar\omega_T}$. This reduction factor also represents coupling to a phonon continuum with an effective frequency $\bar{\omega}_T$. The associated cluster force constant is obtained from $\bar{K}_T = \mu_T \bar{\omega}_T^2$, where μ_T is again the fluorine mass. We will find in Sec. IV that the MnF_6 group in a perovskite lattice is similar to an octahedral molecule in having a much lower force constant for the transverse T_{2g} mode than for the bond stretching A_{1g} and E_g modes. Since the displacements caused by the V_τ will be in units of the effective frequency, a small T_{2g} force can still lead to significant effects in the spectrum.

B. Terms relating to Eq. (3.1b)

$$\mathcal{H}_{so} = -\lambda(\vec{L}\cdot\vec{S}) + \kappa(\vec{L}\cdot\vec{S})^2 + \rho(L_x^2S_x^2 + L_y^2S_y^2 + L_z^2S_z^2)\,. \tag{3.1b}$$

This term[13] allows us to include the spin-orbit interaction to second order within the multiplet. The $\vec{L}\cdot\vec{S}$ term splits the twelve-fold degenerate manifold into three levels. These are twofold, fourfold, and sixfold degenerate, given, respectively, by Γ_6, Γ_8, and $\Gamma_7+\Gamma_8$ for $^4T_1$ and by Γ_7, Γ_8, and $\Gamma_6+\Gamma_8$ for $^4T_2$ in Bethe double-group notation. The reduced matrix element λ is obtained for each configurationally mixed term by using the coefficients obtained from Table II in Eq. (3.7),

$$\begin{aligned}\lambda_{T_1} &= \tfrac{1}{6}\zeta_{3d}(\alpha-\gamma)(\alpha+\gamma-2\sqrt{2}\beta),\\ \lambda_{T_2} &= \tfrac{1}{6}\zeta_{3d}(\alpha+\gamma)(\alpha-\gamma+2\sqrt{6}\beta),\end{aligned} \tag{3.7}$$

where $\zeta_{3d} = 300\ \mathrm{cm}^{-1}$. This is by far the largest contribution to the spin-orbit splitting. The Jahn-Teller effect, however, when present will reduce the importance of this term as it is off diagonal in both E_g and T_{2g} distortions and will therefore be quenched by the two reduction factors, R_E and R_T. The second and third terms give the second-order-spherical and second-order-octahedral spin-orbit interaction. The octahedral term $(L_x^2S_x^2+\cdots)$ induces the full nonmagnetic symmetry of the system and splits the sixfold degeneracy left by the previous two terms into one fourfold and one twofold degenerate level. The κ and ρ coefficients are most accurately obtained by fitting[14] this part of the Hamiltonian to the results of a complete calculation, including spin-orbit, octahedral field, and electrostatic interaction, on the whole d^5 manifold as done by Goode.[15] The necessary coefficients are given in Table III. It should be noted that the octahedral term is diagonal in an E_g distortion (but not in T_{2g}) and becomes important[2] as the first-order term is quenched.

C. Terms relating to Eq. (3.1c)

$$\mathcal{H}_{ex} = 2\mu_B\vec{S}\cdot\vec{H}_{ex}\,. \tag{3.1c}$$

This term brings in the effects of the internal exchange field which leads to the antiferromagnetic ordering at low temperatures. In the molecular-field approximation, it has the form of the Zeeman operator, but acts only on the spins. Since it is diagonal in M_s, taken alone it splits a twelve-fold degenerate ^4T into four sets of three orbitally degenerate states. In the presence of the spin-orbit interaction, no degeneracy is left. In the ground state the exchange field (H_{ex}) for $RbMnF_3$ is[16] about 83 cm^{-1} and is in the direction of the spins. This direction is [111] but it can be changed to the direction of applied stress at values above 0.5 kbar.[17] In a magnetic field above 3 kG along [100] or [111] directions, the spins will flop to [110] directions perpendicular to the field. Since H_{ex} does not commute with the octahedral second order spin-orbit interaction, there should be an energy dependence on the spin direction. Since H_{ex} has no orbital component, it will not be affected by Jahn-Teller distortions.

The simultaneous effects of $\lambda(\vec{L}\cdot\vec{S})$ and $g\mu_B\vec{H}\cdot\vec{M}_s$ in the presence of strong Jahn-Teller effects are illustrated in Fig. 1. The left-hand side corresponds to having only first-order spin-orbit splitting while the right-hand side includes only exchange effects. The center corresponds to the removal of all degeneracy by the collective action of these two effects. If we now add the Jahn-Teller quenching, we shift from the center to the right of the diagram. The ρ-type terms would then be added unquenched to the resultant solutions.

D. Terms relating to Eq. (3.1d)

$$\begin{aligned}\mathcal{H}_{\text{stress}} = {} & V_A' \begin{vmatrix} e_a & 0 & 0 \\ 0 & e_a & 0 \\ 0 & 0 & e_a \end{vmatrix} \\ & + V_E' \begin{vmatrix} \tfrac{1}{2}e_\theta - \tfrac{1}{2}\sqrt{3}\,e_\epsilon & 0 & 0 \\ 0 & \tfrac{1}{2}e_\theta + \tfrac{1}{2}\sqrt{3}\,e_\epsilon & 0 \\ 0 & 0 & -e_\theta \end{vmatrix} \\ & + V_{T_2}' \begin{vmatrix} 0 & e_\zeta & e_\eta \\ e_\zeta & 0 & e_\xi \\ e_\eta & e_\xi & 0 \end{vmatrix},\end{aligned} \tag{3.1d}$$

TABLE III. Coefficients for effective spin-orbit Hamiltonian.

	λ (cm^{-1})	κ (cm^{-1})	ρ (cm^{-1})
$^4T_{1g}$(I)	−29	−3.0	9.1
$^4T_{1g}$(II)	30.7	−1.0[a]	−0.7[a]
$^4T_{2g}$(I)	−33.0	b	b
$^4T_{2g}$(II)	95.5	−2.7	−6.5

[a]Using $Dq = 800\ \mathrm{cm}^{-1}$.
[b]Detailed fit was not necessary for calculations.

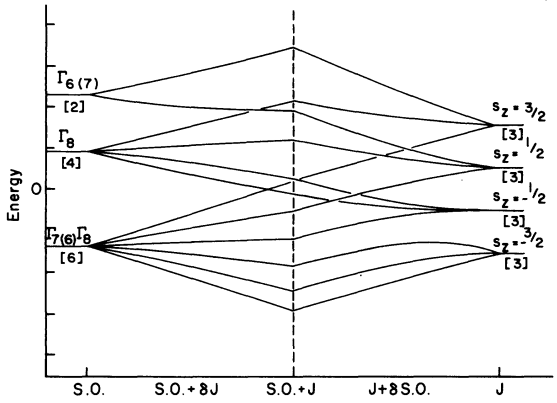

FIG. 1. Correlation between spin-orbit and exchange splitting for a $^4T_{1(2)}$ state. The left corresponds to the spin-orbit effect only (assuming λ to be positive and $\kappa=\rho=0$); the right-hand side corresponds to a pure exchange splitting; the numbers in brackets give the degeneracy. Inclusion of a Jahn-Teller effect corresponds to a shift from the center line to the right on the diagram.

where $e_a=\frac{1}{3}(e_{xx}+e_{yy}+e_{zz})$, $e_\theta=[e_{zz}-\frac{1}{2}(e_{xx}+e_{yy})]$, $e_\epsilon=\frac{1}{2}\sqrt{3}(e_{xx}-e_{yy})$, $e_\zeta=e_{xy}$, $e_\eta=e_{xz}$, and $e_\xi=e_{yz}$. The V'_γ are strain-coupling coefficients analogous to the V_γ of Eq. (3.1a), and both will be discussed in Sec. III E.

The coupling of the Mn^{++} electrons to stress has the same form[11] as the linear coupling to vibrations given in Eq. (3.1a). The e's are defined[18] in terms of compliance constants and stresses as follows, for two important cases:

pressure parallel to [001]:

$$e_{xx}=e_{yy}=S_{12}P, \quad e_{zz}=S_{11}P;$$

pressure parallel to [111]: (3.8)

$$e_{xx}=e_{yy}=e_{zz}=\tfrac{1}{3}(S_{11}+2S_{12})P,$$

$$e_{yz}=e_{zx}=e_{xy}=\tfrac{1}{3}S_{44}P.$$

The resulting strains completely determine the displacements of all the atoms from their normal lattice positions. There are no unknown parameters as there would be for some noncubic crystals. The compliance constants are given in Table IV.

The splitting and shifts of a T state due to applied stress are given in terms of the static coupling parameters V'_γ by

$$\Delta(\text{hydrostatic})=V'_A e_a=\tfrac{1}{3}V'_A(S_{11}+2S_{12})P,$$

$$\Delta(\text{tetragonal})=\tfrac{3}{2}V'_E e_\theta=\tfrac{3}{2}V'_E(S_{11}-S_{12})P, \quad (3.9)$$

$$\Delta(\text{trigonal})=3V'_T e_\xi=V'_T S_{44}P.$$

The quantities measured experimentally, however, are Δ(hydrostatic), $R_T\times\Delta$(tetragonal), and $R_E\times\Delta$(trigonal), the splittings having been reduced by the appropriate Jahn-Teller effects. These quantities are sometimes modified by the presence of sizable spin-orbit interactions as will be discussed in Sec. VII.

E. Coupling coefficients

The two types of coupling coefficients V_γ and V'_γ will be trivially related to each other if only the motions of the nearest neighbors are considered, so that information on one can be used to find the other if this approximation is justified.

Several factors in the $RbMnF_3$ system do justify it. First, Mn has localized $3d$ electrons. Second, the Rb and Mn (second- and third-nearest neighbors) are much heavier than the F atoms and cannot readily follow the high-frequency motions of the latter. The MnF_6 group may therefore act as a molecule, at least for some modes of vibration. Third, the frequency of the most prominent vibrational sideband is definitely higher than the LO_3 lattice mode[2]; this increase could be explained if the force constants in the locale of the excited ion increase, and if most of the lattice motion occurs there. We have also estimated from crystal-field theory that the cube of Rb^+ ions at $\sqrt{3}R$ contributes only 8% as much to the stress response as does the F^- octahedron at R, where R is the MnF bond length, $R=2.125$ Å.

The relations between V_γ and V'_γ if the cluster model is valid are[19,20]

$$V'_A=\sqrt{6}RV_A, \quad V'_E=(2/\sqrt{3})RV_E, \quad V'_{T_2}=2RV_{T_2}. \quad (3.10)$$

The observed stress response can be used to detect the presence of E- and T_2-type Jahn-Teller forces and to tell the direction of motion of the near neighbors resulting from the Jahn-Teller effect, independently of Eq. (3.10). But using Eq. (3.10) allows us to relate the stress response to the dynamic Jahn-Teller effect expressed in Eqs. (3.4)–(3.6). Although the V'_γ are obtained reliably since they depend only on the bulk compliance constants, the reliability of the V_γ is limited by Eq. (3.10).

F. Correlation of theory and experiment

The roots of the Schrödinger equation using Hamiltonian (3.1) should give the relative energies of the 12 substates in a ^4T term, and by varying the

TABLE IV. Compliance constant expressions.[a]

$S_{11}=0.939\times10^{-12}$ cm^2/dyn
$S_{12}=-0.232\times10^{-12}$ cm^2/dyn
$S_{44}=3.03\times10^{-12}$ cm^2/dyn
$(S_{11}-S_{12})P=1.17\times10^{-3}$ kbar^{-1}
$S_{44}P=3\times10^{-3}$ kbar^{-1}
$(S_{11}+2S_{12})P=0.49\times10^{-3}$ kbar^{-1}

[a]Values at 4.2 °K. From R. L. Melcher and D. J. Bolef, Phys. Rev. 178, 864 (1969).

parameters to achieve agreement with the spectrum we should reach an interpretation of the multiplet structure. Although we observe several purely electronic levels, i.e., the magnetic dipole lines, most of these are obscured by the much stronger electric dipole spin-wave sidebands. In Sec. V, we give the experimental evidence that all of the major spectral features are due to the spinwave sidebands or vibrations built upon them. Thus the roots of Eqs. (3.1) will be compared to spin-wave sideband intervals. The intensity of a spin-wave sideband is entirely due to transitions for which $\Delta M_s = -1$. Since the antiferromagnetic ground state is almost entirely ${}^6A_{1g}(M_s = -\frac{5}{2})$, we only observe excited states of the type ${}^4T(M_s = -\frac{3}{2})$. The ratios of the intensities of the sidebands should then be given approximately by the ratios of the squares of the $M_s = -\frac{3}{2}$ component of each substate wave function. The spread of intensity over the 12 sublevels decreases as the Jahn-Teller energy increases, corresponding to a shift to the right in Fig. 1.

The spin-wave sidebands in an ideal case would have a sharp high-energy edge corresponding to the high density of states expected at the Brillouin-zone boundary. Such an example is shown in Fig. 15 where the cutoff is at 70 cm^{-1}. We have evidence, in Ref. 2, that the spacing between the magnetic-dipole line and the corresponding sideband edge does not depend strongly on uniaxial stress.

The spin-wave sidebands, however, do not all have the same shape and therefore we may make an error by assuming that the electronic levels are spaced in the same way as sideband peaks. In two multiplets, ${}^4T_1$(I) and ${}^4T_1$(II), enough magnetic dipole lines were observed to show that no error was made, but small and somewhat uncertain corrections had to be made for ${}^4T_2$(II), Sec. VII, since only one magnetic-dipole line is observed.

In the case of the ${}^4T_1$(I) state, Ref. 2, we found that changes in the spin orientation strongly modify the spin-orbit splitting. These changes inevitably follow the application of small stress or magnetic fields, and in the ${}^4T_1$(II) and ${}^4T_2$(II) states their effects are very large. The solutions of Eq. (3.1) were therefore carried out with several orientations of the exchange field. The spin reorientation phenomenon provided additional experimental data to test the reliability of our calculations.

The solutions of Eqs. (3.1) gave unreduced and reduced multiplet splittings for comparison with experiment, so as to give a Ham reduction factor [Eq. (3.5c)]. The stress response can be used to obtain the corresponding Jahn-Teller force V_τ through Eqs. (3.9) and (3.10). These data lead to the values of the Jahn-Teller energy if the effective force constant and cluster frequency of the lattice are known. These quantities will be obtained in Sec. IV.

IV. EFFECTIVE CLUSTER FREQUENCY AND FORCE CONSTANT

The data obtained in Ref. 2 in the ${}^4T_{1g}$(I) state can be used to provide values for the E_g cluster frequency and the corresponding force constant. We are treating the data for this state in a way that is different than Ref. 2, because it is not appropriate to use the highest lattice fundamental, 470 cm^{-1}, as the cluster frequency, as was done there.

The experimental measurements, interpreted using Eqs. (3.1), give us a reduction factor R_E and a stress response factor V_E'. In terms of the cluster model these can be equated to

$$R_E = \exp(-3E_E/2\hbar\bar{\omega}_E), \quad V_E' = (2/\sqrt{3})RV_E,$$

and

$$E_E = V_E^2/2\bar{K}_E,$$

where $\bar{\omega}_E$ and $\bar{K}_E$ are the effective frequency and force constant for the E-type cluster mode. They are related to each other by

$$\bar{K}_E = \mu_E \bar{\omega}_E^{\,2},$$

where μ_E is the mass of the F atom.[19]

From Ref. 2 we find $E_E/\hbar\bar{\omega}_E = 1.6$ and $V_E = 1.3 \times 10^{-4}$ dyn, giving $\hbar\bar{\omega}_E = 287$ cm^{-1}, $E_E = 458$ cm^{-1}, and $\bar{K}_E = 0.915 \times 10^5$ dyn/cm. These values give $Q_\theta = 0.14$ Å. There are not enough data to give the A_g distortion. The hydrostatic shift of the ${}^4T_1$(I) band is -9.5 cm^{-1}/kbar, but the effective cluster frequency $\bar{\omega}_A$ cannot be found. The value of $\bar{\omega}_A$ should be higher than $\bar{\omega}_E$ and lower than ω_{LO3}, and we have chosen $\bar{\omega}_A = 400$ cm^{-1} as a reasonable estimate (see the discussion in Sec. V G). From $V_A = -2.23 \times 10^{-4}$ dyn, we then find $E_A = 703$ cm^{-1}, $\bar{K}_A = 1.79 \times 10^5$ dyn/cm, and $Q_A = -0.125$ Å.

The values of $\bar{K}_E$, $\bar{K}_A$, $\bar{\omega}_E$, and $\bar{\omega}_A$ just obtained will be used for the analysis of the other ${}^4T$ states. The data for ${}^4T_1$(I) are straightforward, so we consider these values to be reliable.

V. LATTICE VIBRATIONS

The shape of the phonon sideband must contain information about the kinds of local distortions near the excited Mn^{++} ion and in this section we will show how to extract some of this information. The phonon sidebands up to about 500 cm^{-1} from the origins are shown and compared in Fig. 2. In Ref. 2, we gave an interpretation of the shape of the ${}^4T_{1g}$(I) sideband, but here this work will be modified and extended so as to include more details of the Brillouin zone of the phonon branches, and of the way in which the three types of cluster distortions excited these lattice vibrations. We are prevented from carrying out a quantitative treatment of this problem because of the incomplete knowledge of the

phonon dispersion curves. Neutron inelastic scattering data have not yet been obtained for $RbMnF_3$.

Our procedure in this section will be first to show the experimental evidence that the phonon structure is associated entirely with the spin-wave sidebands. Then we write the expressions for the coupling of the cluster distortions to the lattice modes. Next we obtain approximate expressions for the lattice-mode displacements by fitting presently available data to the rigid-ion model of Cowley[21] for the perovskite-type lattice. This fitting helps us to assign the lattice mode spectrum and to obtain qualitatively the coupling strength between cluster distortions and lattice modes. At this point, Fig. 2 can be explained fairly well, and we can say what types of cluster distortions predominate for a given electronic excitation. The rigid-ion model also gives values of the cluster force constant $\bar{K}_E$ in reasonable agreement with the experimental value given in Sec. IV and a value of $\bar{K}_{T_2}$.

A. Spin-wave sideband as spectral origin

There are three experimental indications that the phonons are built on the spin-wave sidebands as their spectral origins: the phonon structure shifts and splits under stress so far as can be seen in the same way as the spin-wave bands; the polarization of the phonon bands under stress follow those of the spin-wave bands; and the temperature dependence of the spectra shows that no odd-parity vibronic origins are present. The first two of these points are covered in Refs. 1 and 2 and will be discussed for the other ^4T states in Secs. VI and VII.

The effects of temperature on the vibrational structure of these transitions are shown in Fig. 3. The prominent structure has a temperature dependence similar to that of the spin-wave origins, that is, both intensity and bandwidth change in the same way. These results are in agreement with the lower-resolution studies of Fujiwara *et al.*[22] Odd-parity vibronic origins would cause a marked increase of intensity with temperature, and this is not observed. Furthermore, they would appear in the spectrum at frequencies higher than the spin-wave frequencies and have a temperature dependence different from the spin waves. These results are further evidence that we need only consider the contributions of even-parity cluster-type distortions A_{1g}, E_g, T_{2g} to the phonon band.

Furthermore, we expect that the regions of the highest density of states in the phonon spectrum will make the major contributions to the electronic spectrum.

B. Lattice-coupling coefficients

In Sec. IV we derived formulas for the forces V_r along the normal modes of an octahedral cluster in terms of parameters which are available from experiment. We will now transform these cluster forces into coupling constants $V_{\vec{q},\lambda}$ to crystal modes $k_{\vec{q},\lambda}$. The corresponding lattice mode distortions are then

$$d_{\vec{q},\lambda} = V_{\vec{q},\lambda}/K_{\vec{q},\lambda}, \tag{5.1}$$

where $K_{\vec{q},\lambda}$ is the force constant for the mode $\vec{q}$, λ. An arbitrary lattice mode can have contributions from three cluster-mode distortions, therefore,

$$V_{\vec{q},\lambda} = \sum_r V^r_{\vec{q},\lambda},$$

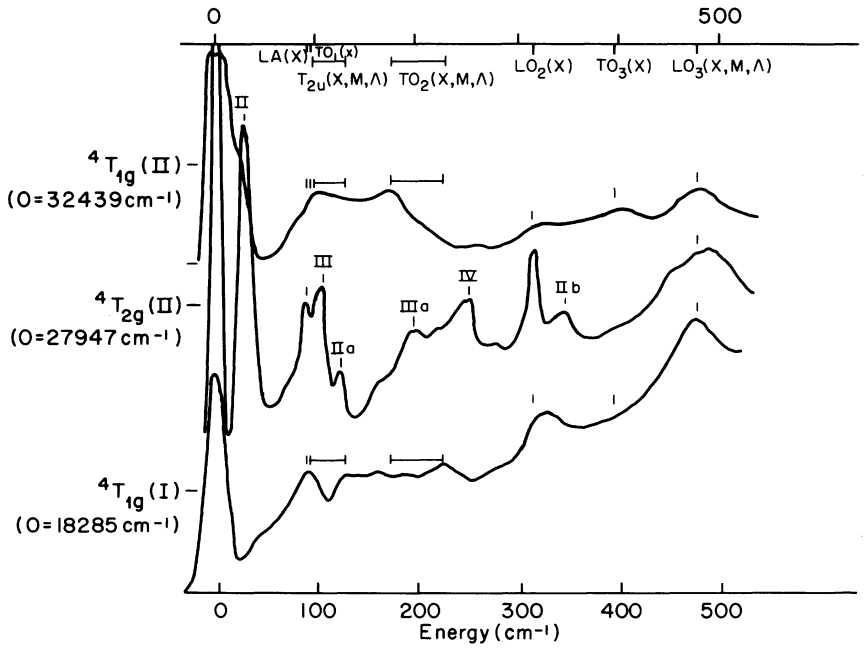

FIG. 2. First 500 cm^{-1} of the three ^4T transitions of $RbMnF_3$ which show structure have been drawn to the same energy scale. Zone edge energies of important lattice modes as discussed in the text have been indicated along the top of the figure. Ordinates are in percent transmission.

where

$$V^{A}_{\vec{q},\lambda}=\left(\frac{M_F}{N\sum_s M_s}\right)2i\frac{1}{\sqrt{6}}\,V_A[\epsilon^{Fx}_{\vec{q},\lambda,x}\sin(\tfrac{1}{2}q_x a)+\epsilon^{Fy}_{\vec{q},\lambda,y}\sin(\tfrac{1}{2}q_y a)+\epsilon^{Fz}_{\vec{q},\lambda,z}\sin(\tfrac{1}{2}q_z a)]\,, \tag{5.2b}$$

$$V^{E}_{\vec{q},\lambda}=\left(\frac{M_F}{N\sum_s M_s}\right)2i\frac{1}{\sqrt{12}}\,V_E[2\epsilon^{Fz}_{\vec{q},\lambda,z}\sin(\tfrac{1}{2}q_z a)-\epsilon^{Fy}_{\vec{q},\lambda,y}\sin(\tfrac{1}{2}q_y a)-\epsilon^{Fx}_{\vec{q},\lambda,x}\sin(\tfrac{1}{2}q_x a)]\,, \tag{5.2c}$$

and

$$V^{T2}_{\vec{q},\lambda}=\left(\frac{M_F}{N\sum_s M_s}\right)2i\tfrac{2}{3}V_{T_2}\frac{1}{\sqrt{4}}\,[(\epsilon^{Fx}_{\vec{q},\lambda,y}+\epsilon^{Fx}_{\vec{q},\lambda,z})\sin(\tfrac{1}{2}q_x a)+(\epsilon^{Fy}_{\vec{q},\lambda,x}+\epsilon^{Fy}_{\vec{q},\lambda,z})\sin(\tfrac{1}{2}q_y a)+(\epsilon^{Fz}_{\vec{q},\lambda,x}+\epsilon^{Fz}_{\vec{q},\lambda,y})\sin(\tfrac{1}{2}q_z a)]\,. \tag{5.2d}$$

Here we assume that the forces act independently of one another and that the electronic part of the wave function can be separated out. The one-phonon sideband shape $G^1(\omega)$ is formed by intensity contributions of amount $S_{\vec{q},\lambda}I_{0,0}$ from each crystal mode $\vec{q}$, λ at an energy $\omega_{\vec{q},\lambda}$ above the zero-phonon line (the spin-wave sideband having intensity $I_{0,0}$), where

$$S_{\vec{q},\lambda}=\left(\sum_s \frac{M_s N\omega_{\vec{q},\lambda}}{2\hbar}\right)d^2_{\vec{q},\lambda}\,. \tag{5.3}$$

Equations (5.1)–(5.3) allow $G^1(\omega)$ to be calculated from the dispersion curves, eigenvectors, and force constants of the lattice and from the cluster forces obtained from the stress data. Lacking the first three requisites, $G^1(\omega)$ cannot be calculated theoretically, nor have we taken the trouble to generate it from the multiphonon sideband by unconvoluting an assumed one-phonon spectrum.[23] Rather, we have taken a more qualitative approach based on obtaining approximate dispersion curves from the work of Cowley[21] on $SrTiO_3$ for which neutron scattering data has been analyzed.

C. Dispersion curves for the lattice modes

The dispersion curves were obtained for the $(q_x, 0, 0)$ wave vectors using a rigid-ion model (Cowley's[21] model I), fitted at zone center to the infrared data of Perry and Young.[24] Although the model is unrealistic in implying $\epsilon = 1$, whereas $\epsilon = 2.5$, we varied the charge so as to give agreement with the Lydanne-Sachs-Teller splitting found from experiment. This procedure has given reasonable results for some simple lattices.[25]

The parameters were varied until a least-squares best fit at $q = 0$ was obtained using the principal oscillator frequencies derived by Perry and Young from their 77° infrared data,[24] and the zone-center LO frequencies and the zone-edge LA and TA frequencies of Young and Perry.[26] Thus the eight parameters are fitted to eight pieces of data. The largest deviation from the observed values was 18 cm^{-1}. The final parameter values are, in Cowley's notation

$$A_1 = 70,\quad B_1 = -12,\quad A_2 = 3.5,\quad B_2 = 2.0.$$

$A_3 = 0.5$ and $B_3 = 0.3$ in units of e^2/v, where v is the volume of the unit cell; and the charges are $Z_{Rb} = 0.8$, $Z_{Mn} = 1.6$, and $Z_F = -0.8$. These parameters give the dispersion curves of Fig. 4. The curves have been displaced so as to match the experimental zone-center energies.

The calculation also gives the polarization vector coefficients necessary for expressions (5.2). The values are listed in Table V, and will be used in later sections.

The calculated dispersion curves lead to assignments of zone edge energies somewhat different from those of Young and Perry,[26] because these authors assumed an NaCl-type negative dispersion of all optical modes in fitting their second-order infrared absorption peaks. We find that the curves calculated from the rigid-ion model show positive dispersions for LO_1 and LO_2 in the [100] directions. This feature also appears in $SrTiO_3$ and is experimentally verified there for LO_1.[21] The calculations also place the T_{2u} branch at 100 cm^{-1} at zone center and 120 cm^{-1} at zone edge. Although the position of this branch is very sensitive to the values of the parameters, it does appear in the low-frequency region in $SrTiO_3$ and in the calculations of Nakagawa *et al.*[27] The main results of the changes proposed here are to bring the T_{2u} branch at [001] to 120 cm^{-1}, and the 311-cm^{-1} energy previously assigned to T_{2u} is now assigned to LO_2 at [001].

Some support for the reassignment is provided by Table VI which shows the infrared combination bands and some second-order Raman-scattering data obtained by us using a 4880-Å gas-laser line. The two-magnon band[28] was observed at 4.2 °K, and the weaker vibrational structure was observed over a range of temperatures. The most prominent peak is at 555 cm^{-1} at 300 °K and increases to 590 cm^{-1} at 80 °K. This same temperature shift was found by Perry and Young[24] for the LO_3 469-cm^{-1} peak (at 85 °K) in the infrared; therefore the 590 peak probably is a combination containing the LO_3 mode. Possible assignments are given for this and other combination bands in Table VI, using the [100] zone-edge energies shown in Fig. 4. Although the assignment of combination bands is a risky procedure, the results are not inconsistent with the zone edge energies of Fig. 4.

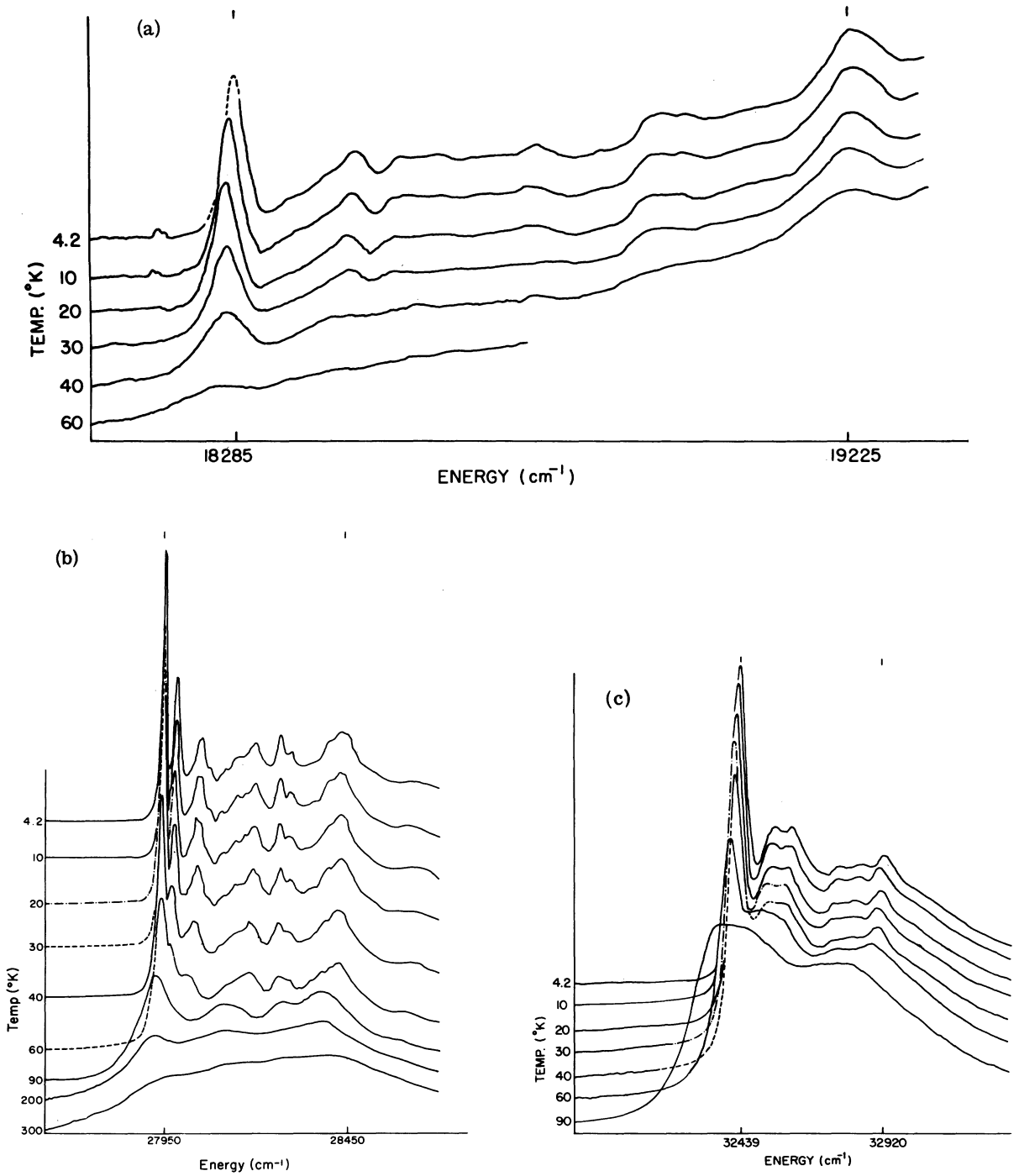

FIG. 3. Variation with temperature of the absorption spectrum (traced on a Cary 14) of the first 500 cm^{-1} of the (a) T_{1g}(I), (b) $^4T_{2g}$(II), and (c) $^4T_{1g}$(II) transitions.

The density of states at the [100] point is supposed to be high and to be a good approximation to the energy of the highest density of states for a given mode.

The results of the vibrational assignment are given at the top of Fig. 2, as the possible energy ranges of the different modes in the phonon sideband.

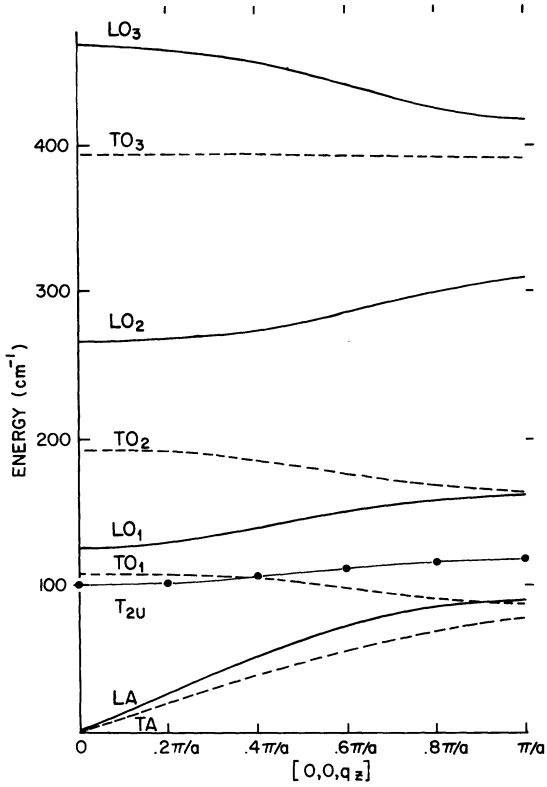

FIG. 4. Calculated $(0,0,q_z)$ dispersion curves for $RbMnF_3$ based on a rigid ion model (Ref. 21) fit at zone center to 80 °K ir data (Ref. 24). The broken lines correspond to transverse modes, the solid lines to longitudinal modes, and the pointed line to the ir inactive T_{2u} at zone center.

D. Contributions of lattice modes to cluster distortions

In this section we want to estimate the most important lattice-mode contributions to the coupling coefficients $V^A_{q,\lambda}$, $V^E_{q,\lambda}$, $V^{T_2}_{q,\lambda}$ of Eq. (5.2). Because of the $\sin(\frac{1}{2}qa)$ factor in the V's, zone-edge contributions are weighted more than interior points. We know the atomic motions best at the points $X(110)$, $M(110)$, and $\Lambda(111)$ on the zone surface because of their high symmetry, and these motions are given by Cowley, Appendix B, Ref. 21. This information tells us how the lattice modes corresponding to different directions of q space contribute to the cluster modes. The contributions of these lattice modes to the intensity of the single-phonon sideband spectrum, $G^1(\omega)$ is determined both by a $\sin^2(\frac{1}{2}qa)$ factor and a density of states. Not having detailed knowledge of the band structure, we assume that there may be contributions from all q directions of the zone to the sideband spectrum. In Table VII we list the lattice modes at high-symmetry points which contribute to given cluster modes. These entries were obtained by noting

TABLE V. $(0, 0, q_z)$ polarization vector components for axial fluorine.

Branch	0	$0.2\pi/a$	$0.4\pi/a$	$0.6\pi/a$	$0.8\pi/a$	π/a
			$\epsilon^F_x z(=y)$			
TO_3	0.389	0.370	0.315	0.23	0.12	0
TO_2	1.56	1.55	1.53	1.44	1.08	0
T_{2u}	2.28	2.17	2.46	2.80	3.01	3.22
TO_1	1.27	1.49	1.08	0.146	0.06	0.22
TA	1.0	0.962	0.84	0.64	0.38	0.00
			$\epsilon^F_z z$			
LO_3	2.65	2.66	2.71	2.82	3.02	3.20
LO_2	1.41	1.43	1.44	1.37	1.01	0
LO_1	0.62	0.62	0.59	0.47	0.25	0
T_{2u}	0	0	0	0	0	0
LA	1.0	0.94	0.78	0.60	0.47	0.42

which atomic motions at a given point in q space contribute to a given cluster motion, and then finding which branches contain that atomic motion. This last step was accomplished by matching the symmetry designations in Appendix B of Ref. 21, with those on the dispersion curves in the figures of Ref. 21. Finally, Cowley's dispersion curves were correlated with ours. For example, at the 001 point for M_2' symmetry there is z motion of the O_I atom corresponding to our $\epsilon^{Fz}_{q,\lambda,z}$. Since we find from Cowley's dispersion curves that both LA and LO_3 have M_2' symmetry at X, these branches have been entered into the E_g column of Table VII.

Table VII shows that the A_{1g} cluster mode contributes to LO_3 in three zone directions and it may be assumed that it contributes to LO_3 over a large fraction of q space. Since LO_3 occurs near 470 cm^{-1} we expect A_{1g} cluster modes to contribute substantial intensity at this energy. The E_g cluster mode contributes to LO_3 at two of the high-symmetry points X and M and will also make contributions near 470 cm^{-1}. The E_g cluster mode begins to disappear from LO_3 and appear in TO_2 as the direction in q space goes away from $[0, 0, q\hat{z}]$, and

TABLE VI. Second-order infrared and Raman peaks.

Observed (cm^{-1})				
ir[a]	Raman		Possible	
LN_2	RT	LN_2	[100] assignments	Calc. (cm^{-1})
200			T_{2u} + TA	200
	220		T_{2u} + (LA or TO_1)	210
333			(LO_1 or TO_2) + (LO_1 or TO_2)	325
	340	335		
420			LO_2 + TA	390
431			LO_2 + (LA or TO_1)	400
	440		$LO_2 + T_{2u}$	430
	555[b]	590[b]		
600			LO_3 + (LO_1 or TO_2)	580
745			$LO_3 + LO_2$	730

[a]Reference 26.

[b]The energy shift on cooling is consistent with that observed for LO_3 in first-order ($q = 0$) ir.

TABLE VII. Zone-edge lattice modes contributing to cluster forces.[a]

A_{1g}	E_g	T_{2g}
$LO_3(X):M_2'$ [b]	$LO_3(X):M_2'$	$T_{2u}T(X):M_5'$
$LA(X):M_2'$	$LA(X):M_2'$	$TO_1(X):M_5'$
$LO_2(M):M_4$	$TO_2(M):M_2$	$TO_2'(M)+T_{2u}T(M):M_5$
$LO_3(\Lambda):\Gamma_2'$	$LO_3(M):M_4$	$T_{2u}L(M):M_1$
$TO_2(\Lambda):\Gamma_{12}'$	$TO_2(\Lambda):\Gamma_{12}'$	$T_{2u}T(\Lambda)+LO_2(\Lambda):\Gamma_{15}$
		$LA(\Lambda)+TO_1(\Lambda):\Gamma_{15}$

[a]Based on $SrTiO_3$ as described in text.

[b]Branch (symmetry point): symmetry of mode at symmetry point.

at the Λ point it contributes only to TO_2. At zone center, TO_2 consists of the motion of the Rb cube against the MnF_6 octahedron, but at Λ it becomes similar to the E_g cluster mode. At zone center, TO_2 has an energy of 194 cm^{-1}. Although we do not know the dispersion of TO_2 for $RbMnF_3$ in the [111] and [110] directions, Cowley's calculations indicate it to be positive for $SrTiO_3$. From these arguments alone we expect A_{1g} and E_g cluster distortions to contribute to $G^1(\omega)$ in the vicinity of 200 cm^{-1}.

Table V samples an important low-symmetry region of the zone and shows how the modes mix when the symmetry restrictions are lifted. It lists the (0, 0, q_z) components of the polarization vector $\epsilon_z^{F_z}$ which contributes equally to A_{1g} and E_g cluster modes [Eq. (5.2)]. These results should give a good indication of the way A_{1g} contributes over the entire zone, and only a fair indication of the contributions of the E_g mode. There is a significant contribution to LO_2, which has no contribution at the high symmetry points of the zone. Therefore, E_g and A_{1g} cluster modes should cause spectral intensity in the LO_2 region near 300 cm^{-1}. The LA mode also has a contribution to the polarization vector throughout the (0, 0, q_z) line, and there should be some intensity near 90 cm^{-1} from both A_{1g} and E_g cluster modes. Since LA involves the heavier Rb motion more than the F motion, this contribution will not be large, as shown by the values in Table V when weighted by the $\sin(\frac{1}{2}qa)$ factor.

To summarize, the A_{1g} and E_g cluster modes should contribute spectral intensity predominantly at 470 cm^{-1} and some at 300, ~200, and 90 cm^{-1}.

The T_{2g} cluster mode is seen from Table VII to contribute at zone edge to the lower energy modes, predominantly T_{2u} which the calculations have indicated to be near 120 cm^{-1} at X and probably near this energy for other directions (in $SrTiO_3$ this mode shows positive dispersion for [110] and [111][21]). Table V shows that the most striking mixing at interior points of the zone is with T_{2u}, TO_2, and TO_1, decreasing in that order. The major contributions to $G^1(\omega)$ from a T_{2g} cluster distortion should then be expected in the region of 100–200 cm^{-1}.

E. Assignment of peaks in the phonon sidebands

It was seen in Ref. 2 for the $^4T_{1g}$(I) state, and will be shown for the other states that a progression of peaks at approximately 470 cm^{-1} is the dominant feature of the sidebands. This frequency corresponds to the LO_3 mode raised somewhat in the excited states, probably because of changes in the electron distributions compared to the ground state. The predominance of LO_3 means that A_{1g} and E_g cluster modes are strongly excited, according to the analysis of Sec. V D.

Figure 2 shows the structure of the phonon sidebands for $^4T_{1g}$(I), $^4T_{2g}$(II), and $^4T_{1g}$(II) up to about 500 cm^{-1}, the one-phonon region. The spectra have been drawn to the same scale with the first spin-wave sideband at zero on the wave number scale. In Sec. VII, we show that $^4T_{2g}$(II) has four intense-spin-wave-sideband origins. Origins II, III, and IV are indicated in Fig. 2 along with some of their prominent phonon sideband structure. Other structure belongs to origin I at zero, and only this structure will be referred to in making comparisons with the other spectra. Both $^4T_{1g}$(I) and $^4T_{2g}$(II) have the 470-cm^{-1} peak as their most intense feature. The other prominant features in both spectra are (a) the peak at 315 cm^{-1}, which is at the correct energy to be LO_2; (b) the peak at 90 cm^{-1}, having an energy and shape identifying it as the LA mode; (c) the weaker overlapping structure between 130 and 230 cm^{-1}, which is probably composed of contributions from many branches. TO_2 could be contributing near 200 cm^{-1}. The similarity between $^4T_{1g}$(I) and $^4T_{2g}$(II) in this region is made very clear by the σ-polarized spectrum of $^4T_{2g}$(II) under trigonal stress, shown at the top of Fig. 16, where the sidebands of origin I make the only large contributions to the spectrum, and III and IV origins are suppressed. We note that all prominant structure in the phonon sidebands for $^4T_{1g}$(I) and $^4T_{2g}$(II) is assignable to lattice modes predicted to contribute to $G^1(\omega)$ when the cluster distorts along the A_{1g} and E_g modes.

If we now look at $^4T_{1g}$(II) we see that the most prominent structure is in the 100–180-cm^{-1} region, in contrast to what we have found for the other two transitions, which show the least vibrational activity in this region. The 470-cm^{-1} peak still appears but is no longer dominant. We will see in Sec. VI that there are no origins other than the composite broad one at 0 cm^{-1}. The 100–180-cm^{-1} region is, however, the energy region which contains the lattice modes we expect to be excited in $G^1(\omega)$ by a

T_{2g} cluster distortion. [We also note the presence of a much weaker peak at 408 cm^{-1}, close to the value of TO_3 which should have (Table V) small contributions from a T_{2g} cluster mode.] This prominent structure is evidence that a T_{2g} distortion occurs in the $^4T_{1g}$(II) state along with $A_{1g}+E_g$. The T_{2g} force does not have to be large relative to the $A_{1g}+E_g$ force to give comparable spectral intensity as the intensity is inversely proportional to the mode force constant and frequency, and these are smaller for the T_{2g} mode than for the A_{1g} and E_g modes.

F. Intensity of the LO_3 mode

The description just given of the one-phonon sideband intensity $G^1(\omega)$ must remain qualitative until the full dispersion curves and their associated eigenvectors are found. For the LO_3 mode, however, we feel it is justified to make an approximate calculation of $G^1(\omega_{LO_3})$. The LO_3 branch is in an isolated region of energy, so we do not expect much mixing with other modes anywhere in the zone. Cowley finds for $SrTiO_3$ that the dispersion in three directions in q space is negative, and not large, and we will assume that these indications apply to $RbMnF_3$. These conditions justify making the Huang-Rhys approximation[29] for the LO_3 branch. We can then insert Eqs. (4.2b) and (4.2c) into Eq. (4.1) and then into Eq. (4.3) and sum directly over the entire zone, only making the approximation that the magnitude of the polarization vector is a constant. Then with $\omega_{LO_3}=470$ cm^{-1} for all q, we obtain the intensity contribution to $G^1(\omega)$ at 470 cm^{-1}:

$$G^1(\omega_{LO_3})=I_{00}S_{LO_3}, \tag{5.4a}$$

where

$$S_{LO_3}=\bar{\epsilon}^2_{LO_3}\left(\frac{V_A^2+V_E^2}{2K_{LO_3}}\right)\Big/\hbar\omega_{LO_3} \tag{5.4b}$$

and $(\bar{\epsilon}_{LO_3})^2$ is the average value of

$$(M_s/\textstyle\sum_s M_s)(\epsilon^{F_g}_{q,LO_3,x})^2$$

over the entire zone. This is a number which becomes less than unity as the $A_{1g}+E_g$ distortions mix into the lower branches. It is found from Table V to be about 0.9, using the LO_3 row. The assumption made here is that the [100] direction is representative of the entire zone. From section d and Table VII, this is seen to be a fairly good approximation for the A_{1g} cluster mode coupling, but not as good for the E_g coupling.

In Ref. 2 we used a q^2 weighting factor to extend our one-dimensional rigid ion solutions to include the whole zone. This was incorrect as it led to an incomplete Fourier analysis of the distortion.

Since for T_{1g}(I), V_A is much larger than V_E, we will not make much error in this state when applying Eq. (5.4). Therefore, we use $\bar{\epsilon}^2_{LO_3}=0.9$; we find K_{LO_3} from $\omega_{LO_3}=470$ cm^{-1} and $\mu_{LO_3}=3.1\times10^{-23}$ (since almost the entire reduced mass throughout the zone is that of the F atom) to give $K_{LO_3}=2.48\times10^5$ dyn/cm; and finally we use the values of V_A and V_E obtained from the stress experiments of Ref. 2 (their values are given in Sec. IV). The result is $S_{LO_3}=1.3$. In Fig. 5, $G^1(LO_3)$ is drawn in, and it is seen to be consistent with the appearance of the spectrum. The values of V_A and V_E must be approximately correct for this level of agreement. It is important to note V_A and V_E depend on the assumption of the cluster model contained in Eq. (3.10), but that Eqs. (5.4a) and (5.4b) do not depend on the cluster force constants or frequencies of Sec. IV. Thus, the V's obtained through (3.10) are here shown to be approximately correct because of the reasonable size of $G^1(\omega_{LO_3})$, independent of other assumptions. In the sections on the $^4T_{1g}$(II) and $^4T_{2g}$(II) states, we will demonstrate this argument for these cases as well.

G. Theoretical estimates of cluster force constants

An estimate of the force constant $\bar{K}_E$ or $\bar{K}_A$ can be obtained from the force on a fluorine due to its displacement along the Mn-F axis using the parameters of the rigid-ion model. This force is given by $(e^2/v)(Z_F^2C^{\parallel}_{FF}+2B_2+A_1+2A_3+2B_3)$ and is 1.36×10^5 dyn/cm if we use -47 for $C^{\parallel}_{FF}$, a zone-center Coulomb coefficient which omits the macroscopic field. This value corresponds to a cluster frequency of 350 cm^{-1}. In Sec. IV we obtained an experimental value for the E_g cluster force constant of 0.92×10^5 dyn/cm and a corresponding effective frequency of 287 cm^{-1}. This frequency is consistent with the spread of energies we find for the lattice modes onto which V_E projects (see Table VII). The A_{1g} effective frequency will be higher as the major contributions are from the LO_3 branch (Table VII). A reasonable estimate is 400 cm^{-1} with a corresponding force constant of 1.79×10^5 dyn/cm. The T_{2g} effective force constant can be similarly approximated by the force on a fluorine due to its displacement perpendicular to the Mn–F bond. This is given by $(e^2/v)(Z_{FF}^2C^{\perp}_{FF}+A_2+B_1+B_2+A_3+3B_3)$. In contrast to the axial case, the transverse Coulombic term is repulsive while the short-range terms are attractive. Using $C^{\perp}_{FF}=17.2$, gives $K_T=2\times10^4$ dyn/cm and an associated cluster frequency (using a reduced mass equal to that of fluorine) of 135 cm^{-1}. The fair agreement between the calculated and experimental values of $\bar{K}_E$ leads us to believe that the calculated values of $\bar{K}_T$ must be reasonably correct.

In Ref. 2 we used a value of 6.4×10^4 dyn/cm taken from Ref. 27. This value is obtained using the Wilson F-G matrix formalism to fit observed infrared frequencies. Such a model is unrealistic, as it does not take into account the long-range Coulombic

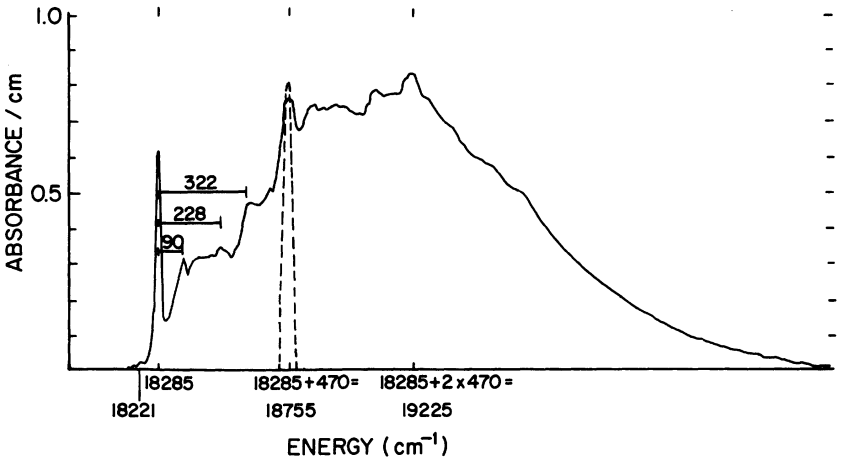

FIG. 5. Absorption spectrum of the $^4T_{1g}$(I) transition. The dotted line presents the 18 285-cm^{-1} spin-wave sideband increased in intensity by a factor of 1.3. Frequencies of other structures have been shown at higher resolution in Ref. 1.

terms and therefore does not give the ionic splitting of the longitudinal and transverse branches (see dispersion curves in the Appendix of Ref. 30).

VI. $^4T_{1g}$(II)

A. Experimental observations

The complete spectrum of the $^4T_{1g}$(II) transition starting near 3100 Å is shown in Fig. 6. There are two magnetic-dipole (MD) lines of about equal intensity which act as origins to the spin-wave sidebands. They have the energies 32 367 and 32 380 cm^{-1} (a 13 ±2-cm^{-1} splitting) and are shown in Fig. 7(a) for a 2-cm crystal. These MD lines are too weak and broaden too quickly under stress for use in the study of the effects of different perturbations. This problem is overcome by using the more intense composite spin-wave sideband shown in Fig. 7(b). However, the components of the sideband have the disadvantage that they overlap because of spin-wave dispersion, and this introduces some error in determining their energies. Three spin-wave sidebands are contained in the composite sideband, each about 66 cm^{-1} higher in energy than its MD origin. The higher two sidebands are located 12 and 29 cm^{-1} above the first. The three sidebands correspond to the three predominantly $M_s = -\frac{3}{2}$ exchange levels. They will be referred to as I, II, and III in order of increasing energy.

Most of the changes brought about by uniaxial stress occur in the relatively sharp spin-wave sidebands, although for 1.5 kbar along [100] in π

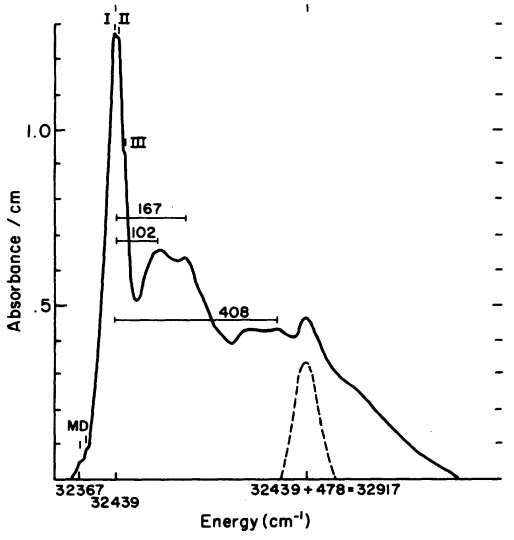

FIG. 6. Absorption spectrum of the $^4T_{1g}$(II) transition. *MD* indicates the two observed magnetic dipole lines. I, II, and III label spin-wave sidebands. The dotted curve represents the composite spin-wave sideband (I+II+III) reduced in intensity by a factor of 0.25 and increased in energy by 478 cm^{-1}.

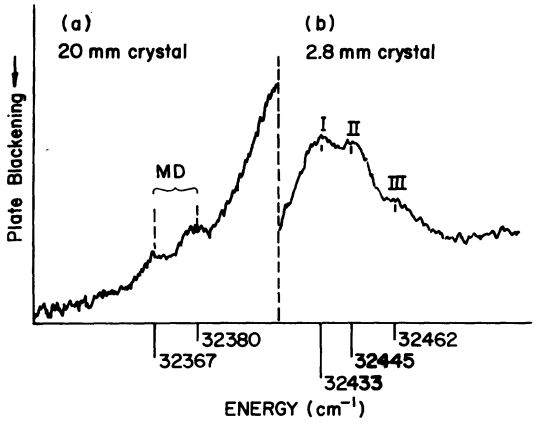

FIG. 7. Microdensitometer tracing of (a) magnetic-dipole lines using a 20-mm crystal and (b) the composite sideband using a 2.8-mm crystal for $^4T_{1g}$(II).

polarization the 102-cm^{-1} band is observed to split slightly, reflecting the behavior of the composite origin. We find no evidence for substantial intensity associated with higher multiplet components contained in the vibronic-sideband envelope. When considered together with the temperature dependence (Sec. V), these results show that only the linear coupling terms of Eq. (3.1a) are responsible for the sideband structure.

We found in Sec. V that only for the transition to $^4T_{1g}$(II) does the vibrational sideband show prominent structure in the 100–170-cm^{-1} region, indicating the excitation of a T_{2g} cluster distortion. Further confirmation of the T_{2g} distortion will be found in the interpretation of the response to stress. An A_{1g} and an E_g distortion must also be excited as shown by the appearance of the 478-cm^{-1} longitudinal mode.

Figure 8 shows the [100] stress response of the composite spin-wave sideband up to 3 kbar. The results are summarized in Fig. 9 (the large error is due to the difficulty in analyzing the overlapping bands). We see that as the stress increases, the lowest-energy sideband I remains present in both polarizations and increases in energy with increasing stress at a rate of 8.7 ± 1.2 cm^{-1}/kbar. Band II becomes completely σ polarized and first increases in energy by about 13 cm^{-1} at $\frac{1}{2}$ kbar, due to the reorientation of spins toward the direction of stress. As the stress increases, this band then moves downward with a slope of -7 ± 1.5 cm^{-1}/kbar and, at a stress of about 1.5 kbar, substantially overlaps band I, which has been moving upward in energy. These bands can, however, be resolved since I also appears in π polarization and can therefore be approximately subtracted; but this procedure leads to a somewhat inaccurate value for the stress response. The 29-cm^{-1} shoulder III is seen to shift downward by several wave numbers and to become π polarized as the stress approaches $\frac{1}{2}$ kbar. It then shifts upward with a slope of 6.2 ± 1.2 cm^{-1}/kbar. Thus two levels are moving upward in energy in a somewhat less than parallel manner with an average slope of 7.4 ± 1.2 cm^{-1}/kbar; one is moving downward with a -7 ± 1.5 cm^{-1}/kbar slope. These results give a hydrostatic shift upward in energy by 2.7 ± 1.3 cm^{-1}/kbar and a tetragonal splitting of -14.2 ± 2.7 cm^{-1}/kbar, the Z component decreasing in energy.

Figure 10 shows the effects of increasing trigonal stress on the composite sideband. The results are summarized by the plot in Fig. 11. We find two σ-polarized components moving upward in energy with increasing stress with an average slope of 3.9 ± 1.5 cm^{-1}/kbar and a π-polarized sideband which is almost unaffected by the [111] stress ($\partial E/\partial S = +0.25 \pm 1$ cm^{-1}/kbar). These give a hydrostatic shift upward by 2.7 ± 0.9 cm^{-1}/kbar and give a trigonal splitting of -3.6 ± 1.5 cm^{-1}/kbar, the z component moving downward.

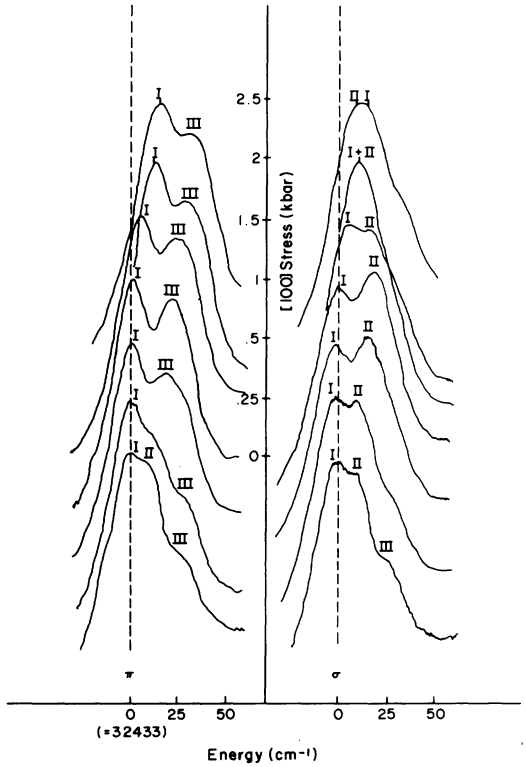

FIG. 8. High-resolution microdensitometer tracings of the effects of a [100] stress on the composite spin-wave sideband of $^4T_{1g}$(II). Read ordinate from top of peak.

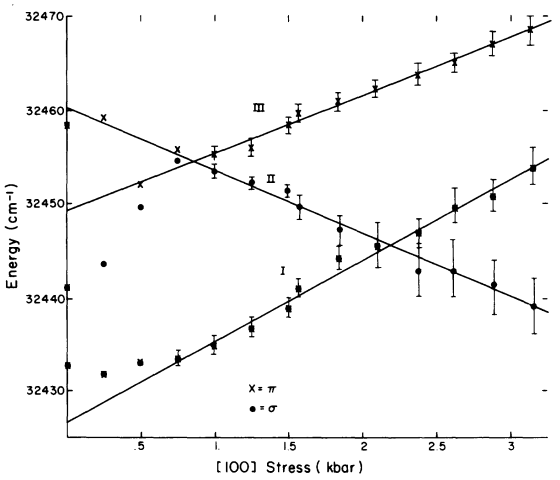

FIG. 9. Plot of the [100] stress response of the $^4T_{1g}$(II) composite spin-wave sideband. The error bars indicate the increase in difficulty in curve resolution of the overlapping bands. The curves are least-square fit to error weighted points.

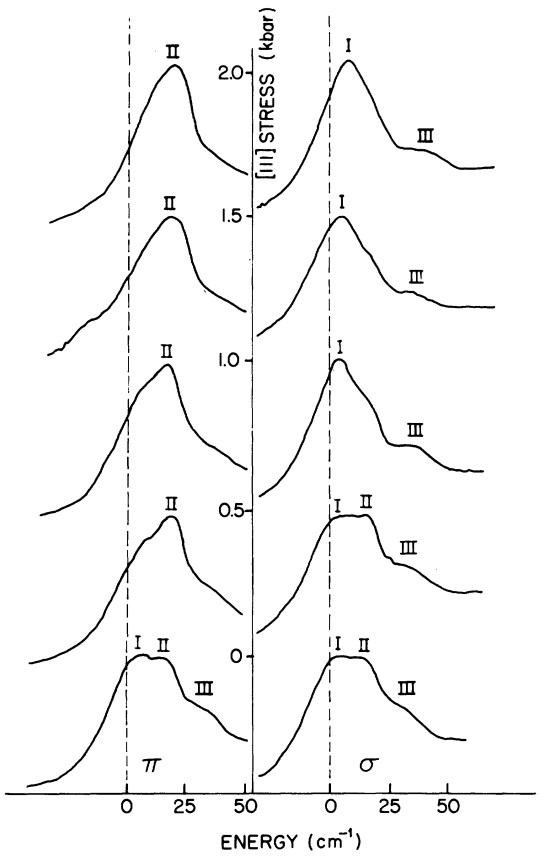

FIG. 10. Microdensitometer tracing of the effects of a [111] stress on the composite sideband of $^4T_{1g}$(II). Read ordinate from top of peaks.

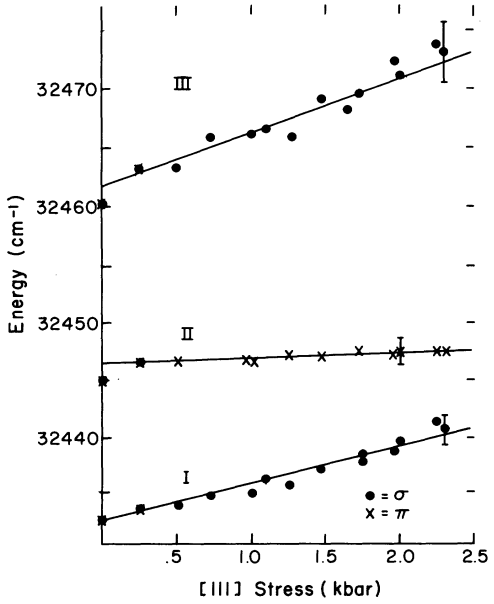

FIG. 11. Plot of [111] stress response of the $^4T_{1g}$(II) composite spin-wave sideband.

Illustrated in Fig. 12 is the axial spectrum in a magnetic field applied in the [100] direction (the same spectrum is observed in the [111] direction). There is a gradual shifting of the sidebands in fields up to about 8 kG, with no dependence of energy on field above this value. This maximum splitting is represented by the 15-kG plot, on which II has moved up to 15.5 cm^{-1} and now blurs out the 29-cm^{-1} shoulder. The shoulder does not, however, seem affected much by field at the lower fields where it is still resolvable.

We conclude this section by summarizing the spin-reorientation effects. The [111] spin-orientation data were obtained from the unperturbed system; the [011] orientation data from the spectrum in a [100] magnetic field which flops the spins into [011] directions perpendicular to the applied field; and the [100] spin-orientation data from the stress response data of Fig. 9 extrapolated to zero. The spectral effects are illustrated by the low-stress spectra of Figs. 8 and 10, and are collected in Table VIII. We find that the energy of the second level increases while that of the third sideband decreases upon changing the orientations of the spins from [111] to [110] to [100].

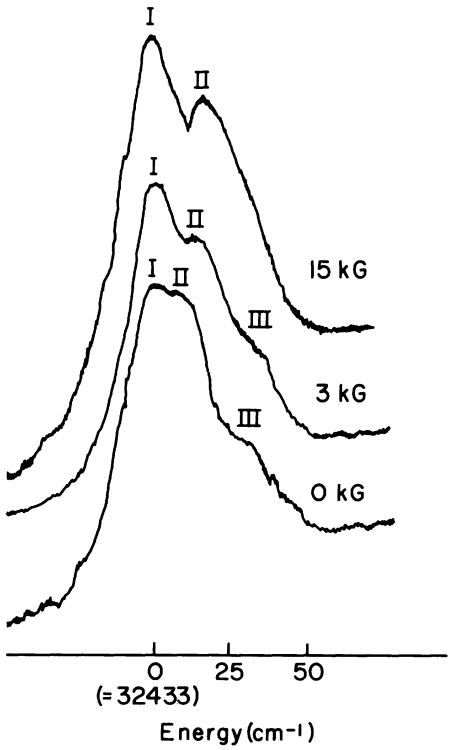

FIG. 12. Microdensitometer tracing of the effects of a [111] axial magnetic field on the composite spin-wave sideband of $^4T_{1g}$(II).

B. Energy calculations (including Jahn-Teller effects)

Using the spin-orbit–plus–exchange part of Hamiltonian (3.1), with the parameters given in Table III and with the exchange field in the [111] direction, we calculate the spacing of the lowest three substates (those which we expect to have the most intense spin-wave sidebands based on their predominantly $M_s = -\frac{3}{2}$ character) to be 29 and 65 cm^{-1} above the first. This separation is considerably larger than that which was observed (Fig. 6). Due to the spin-orbit mixing, our calculation also predicts a spread of $M_s = -\frac{3}{2}$ character over the exchange levels of higher energy which have predominantly $M_s = -\frac{1}{2}$ character. Sizable distribution of intensity corresponding to this calculation is not observed. Both the lower observed splitting and the concentration of intensity in the lowest-three spin-wave sidebands show that the spin-orbit coupling has been reduced.

We therefore want to explain the observed splittings and the response to stress through the inclusion of Jahn-Teller distortions, and here we outline our procedure. We first attempt to explain the results using an E_g distortion only. The E_g Jahn-Teller energy calculated from the experimental [100] stress response turns out, however, to be less than half of that calculated from the spin-orbit quenching. This discrepancy indicates that the [100] stress response has also been quenched and therefore we include a T_{2g} distortion (the presence of which has been indicated by the lattice modes contributing to the phonon sideband (Sec. V E). This result is in agreement with the crystal field calculations discussed in Sec. X, and Table XII, which predict the trigonal splitting to be largest for $^4T_{1g}$(II). Values for both the T_{2g} and E_g Jahn-Teller reduction factors are then found which reproduce the spin-orbit splitting and the observed stress reponses.

Since both kinds of distortion are probably present, we will analyze the experimental data with the following formulas for the reduction factors R, and static coupling constants V':

TABLE VIII. Multiplet spacings in cm^{-1} for different spin directions for $^4T_{1g}$(II).

		Spin direction [111]	[110]	[100]
Experimental values	III	~29	~29	22
	II	13 ± 2	15.4	31
	I	0	0	0
Calculated[a] values	III	29.4	29.2	28.7
	II	13.8	15.1	17.8
	I	0	0	0

[a]Using $R_E R_{T_2} = e^{-1.1}$ and the $E_g - G(X)$ terms corresponding to $X = 0.565$.

$$R^{so}(\text{expt}) = R_E^{so} R_T^{so}, \tag{6.1}$$

$$V'_E(\text{expt}) = R_T V'_E, \tag{6.2}$$

$$V'_T(\text{expt}) = R_E V'_T. \tag{6.3}$$

These formulas imply that the E and T_2 quenching effects can be treated as independent of each other, as is the case when both reduction factors are not much less than one.[31]

We begin by assuming that $R_T = 1$. Figure 13 shows the Ham E_g-quenching calculation for the lowest three levels with the exchange field in the [111] direction. The observed spacings of 13 and 29 cm^{-1} are fitted well by $E_E/\hbar\bar{\omega}_E = 0.72$. This gives $R^{so}(\text{expt}) = e^{-1.08} = 0.33$. For these values the spin-orbit mixing of the exchange levels is very small, and the observed retention of intensity in the lowest-three levels is explained. Using the cluster frequency $\bar{\omega}_E$ of Sec. IV gives $E_E = 200$ cm^{-1}.

We can now use the tetragonal stress response as in Ref. 2 to obtain another value of E_E through Eqs. (3.9), (3.10), (3.5b), and the cluster force constant of Sec. IV. The response to [100] stress is -14.2 ± 2.7 cm^{-1}/kbar, Fig. 9, leading to $E_E = 117$ cm^{-1}. The disagreement with the value of 200 cm^{-1} shows that $R_T < 1$. The unquenched value of the splitting would be 19 cm^{-1}/kbar, much larger than the observed splitting.

Since both R_T and R_E are less than 1, we need the trigonal stress data so as to bring in Eq. (6.3) and to be able to solve for both reduction factors. The [111] stress splitting of -3.6 cm^{-1}/kbar must reflect a value of R_E less than 1, according to Eq. (6.3).

The manipulation of the data is done with the following definitions of the reduction factors:

$$-R_E = \exp\left[\frac{-3E_E}{2\hbar\bar{\omega}_E}\right], \quad R_T = f\left(\frac{E_T}{\hbar\bar{\omega}_T}\right), \quad R_T^{so} = \exp\left[\frac{-9E_T}{4\hbar\bar{\omega}_T}\right],$$

where ω_E and ω_T are the cluster frequencies and f is a function graphed by Caner and Englman[12]: and with the relations $E_E = V_E^2/2K_E$, $E_T = 2V_T^2/3K_T$. From Eqs. (3.9) and Table IV we obtain the V' from the stress data:

$$-14.7 \text{ cm}^{-1}/\text{kbar} = \tfrac{3}{2} V'_E \times 1.17 \times 10^{-3} \times R_T,$$

$$-3.6 \text{ cm}^{-1}/\text{kbar} = V'_T \times 3 \times 10^{-3} \times R_E$$

and from Eq. (3.10) we obtain the V's in terms of the data and the reduction factors. Then we can obtain E_E and E_T as functions of the reduction factors and the K's. The K_T is given in Sec. V G, and is a partly theoretical value based on the rigid ion model. The K_E is experimental, and is discussed in Sec. IV, but is consistent with the rigid-ion model. Finally, we must find the E and R values consistent with the definitions of the R given above.

The values obtained are $E_E = 143$ cm^{-1}, $E_T = 21.6$ $R_E = 0.47$, $R_T^{so} = 0.70$. So far we have only used Eqs. (6.2) and (6.3). Now we note that the value of $R_E^{so} R_T^{so}$

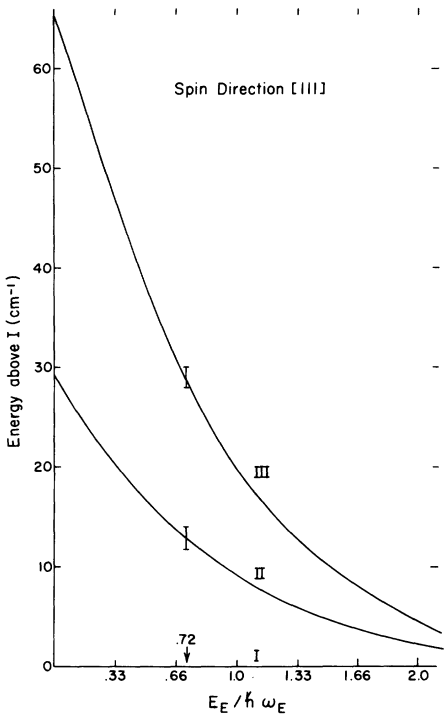

FIG. 13. Ham effect spin-orbit–plus–exchange calculation of the spacings of the lowest three sublevels of $^4T_{1g}$(II) with the spins in the [111] directions. Error bars indicate the experimentally observed spacings and correspond to a value of $E_E/\hbar\omega_E = 0.72$.

from these equations equals 0.33, which is in agreement with the value of R^{so}(expt), and therefore Eq. (6.1) is also satisfied. Thus, we have obtained a pair of Jahn-Teller energies consistent with all the data.

Let us summarize the evidence for the presence of the T_{2g} Jahn-Teller distortion. First there is the reduction of the tetragonal stress splitting. Second, the large trigonal splitting in the presence of this E_g spin-orbit reduction factor means that there is a large T_{2g} force [Eq. (3.10)]. Third, there is the presence of phonon modes which can only be excited by T_{2g} cluster distortions. Fourth, crystal-field theory predicted the largest T_{2g} stress response of any state (see Sec. X, Table XII).

C. Verification of the multiplet assignments

The final calculation of the multiplet energies and intensities, using the reduction factors just found, give the positions of the first three sidebands correctly, and give the third sideband 5% less intensity than the first two. All of the missing intensity goes to the sidebands of the next exchange triplet near 100 cm^{-1}. In fact, the third sideband is about 20% weaker than the first two, in approximate agreement with the calculations. This intensity should appear in the 100-cm^{-1} region, but the broad band at 102 cm^{-1} seems far too strong to be due to the higher sidebands, and we must retain its original assignment as the T_{2g} mode. This conclusion is in further support of our entire analysis of the $^4T_{1g}$(II) band.

So far we have only used the multiplet pattern when the exchange field is oriented along [111]. The spin reorientation effects in this state are somewhat unusual and had to be investigated to show that the analysis in Sec. VI B was correct. In the crystal-field energy region near $Dq = 780$ cm^{-1}, a ^2E state (Γ_8) lies very close to $^4T_1$(II), and perturbs its two Γ_8 sublevels.[15] Thus the spin-orbit splitting is very sensitive to the values of B, C, Dq, and ζ_{3d}. A second complication is that the in-state second-order vibronic terms can be large for the small values of E_{JT} in this case. These arise from the interaction of $\mathcal{H}_{vib}$ and $-\lambda\vec{L}\cdot\vec{S}$. Ham[11] gives a closed form for the E_g vibronic interaction, but not for the T_{2g} interaction, and the only thing we know about the latter is that it has octahedral symmetry. Thus there are three terms contributing to the coefficient of $L_x^2S_x^2 + L_y^2S_y^2 + L_z^2S_z^2$, the two in-state vibronic terms and the second-order out-of-state spin-orbit term.

Using only the ρ value of Table III (for $Dq = 800$ cm^{-1}, because we could not interpolate for $Dq = 780$ cm^{-1} (in Ref. 15), and the combined reduction factor of 0.33 of Sec. VI B, we get the multiplet splittings for different spin directions shown in Table VIII. The calculation for the [100] direction does not agree well with the experimental multiplet spacing. To take account of the contributions from the other factors which cannot be obtained *a priori*, we increased ρ from -2.1 to -8.1. With the new ρ value, the calculation reproduces the multiplet spacings within experimental error. This result shows that the reduction factor obtained earlier for the [111] spin direction is practically unaffected by the increase of ρ. The calculated splittings for the [111] spin direction are I–II = 12.4 and I–III = 30.2 cm^{-1}, and so are practically unaffected by the use of the new ρ value. For the [100] direction in particular, the calculations using the new ρ value agree with the experimental values of Table VIII.

D. Distortions and Franck-Condon factors

Using $V_E = -0.88\times10^{-4}$ dyn, which corresponds to the unquenched tetragonal splitting of -19 cm^{-1}/kbar, we calculate the displacement in the Q_θ mode to be -0.095 Å, a contraction along the z axis, and an expansion by half as much along the x and y axes. The A_{1g} force is similarly found to be 0.70×10^{-5} dyn. The corresponding displacement in the Q_A mode is 0.039 Å (using $\hbar\omega_A = 400$ cm^{-1}), an axial expansion outward. This corresponds to the energy

$E_A = 70$ cm^{-1}. From these forces and Eq. (5.4d) we find the Franck-Condon factor of the LO_3 lattice mode to be 0.25. The composite spin-wave sideband reduced in intensity by this factor is included in Fig. 6 at 470 cm^{-1}. Since a significant portion of $V_A^2 + V_E^2$ is due to the E_g mode, this is probably an overestimate as discussed in Sec. V.

The -8.0-cm^{-1}/kbar unquenched trigonal splitting gives a T_{2g} force of $V_T = -0.122 \times 10^{-4}$ dyn. Although this force is small, the T_{2g} force constant (2×10^4 dyn/cm) is significantly less than for the A_{1g} or E_g modes, so we obtain T_{2g} distortions of 0.04 Å (Q_ξ, Q_η, Q_ζ) from Eq. (3.6a). We do not attempt to calculate contributions to $G^1(\omega)$ from individual lattice modes because 100–170 cm^{-1} is a very complex region of the phonon spectrum and the T_{2g} cluster mode projects onto many crystal modes of different energy. However, since this energy distribution is not large, we can approximate the overall intensity contribution in this region by the cluster T_{2g} Franck-Condon factor $S_T = E_T/\hbar\omega_T = 0.19$. We find the over-all intensity to be between $0.4 I_{0,0}$ and $0.7 I_{0,0}$ depending on how the regions are divided, which is in reasonable agreement with the appearance of the spectrum shown in Fig. 6.

VII. $^4T_{2g}$(II)

A. Experimental observations

A medium resolution spectrum of the $^6A_{1g} \rightarrow {}^4T_{2g}$(II) transition at 2 °K is shown in Fig. 14, and a higher resolution tracing of the first 100 cm^{-1} in Fig. 15. Figure 15 shows one sharp, weak magnetic dipole line at 27 877.3 cm^{-1}, with a characteristically shaped spin-wave sideband (I) having a sharp cutoff at 69.3 cm^{-1} above the magnetic-dipole line built onto it. Another probable spin-wave sideband (II) with a more symmetrical shape and a peak 28.2 cm^{-1} above the cutoff of the first is also shown in Fig. 15. The polarized [100] and [111] stress response of the complete transition is shown in Fig. 16 (the structure is calibrated in Fig. 17). This response clearly confirms II as a new electric dipole origin, because while the lowest sideband appears in both polarizations, II is only σ polarized and has shifted upwards by about 20 cm^{-1}. The polarized-stress data also reveals a third sideband (III) at 102 cm^{-1} appearing only in π polarization with a large downward shift of about 40 cm^{-1} under [100] stress. The shift and polarization of III allow it to be separated from the other two prominent peaks in the 80-to-125-cm^{-1} region. The 87- and 122-cm^{-1} peaks (Ia and IIa) then remain. They show the same behavior as the first two origins under stress and are thus the totally symmetric LA (90 cm^{-1} at zone edge) built upon the two spin-wave sideband origins.

It is hard to interpret all the stress effects that occur in the region of the bands overlapping between 150 and 250 cm^{-1}. However, the most intense peak, IV, which lies at 248 cm^{-1}, is unchanged in energy but under both directions of stress appears strongly only in the π polarization. It cannot be caused by totally symmetric vibrations built onto any of the aforementioned three origins since it does not show the same polarization and energy shift as any of these three. It has the same polarizations under stress as III but does not undergo the large shift to lower energy which this third origin exhibits. Also the fact that it is a dominant

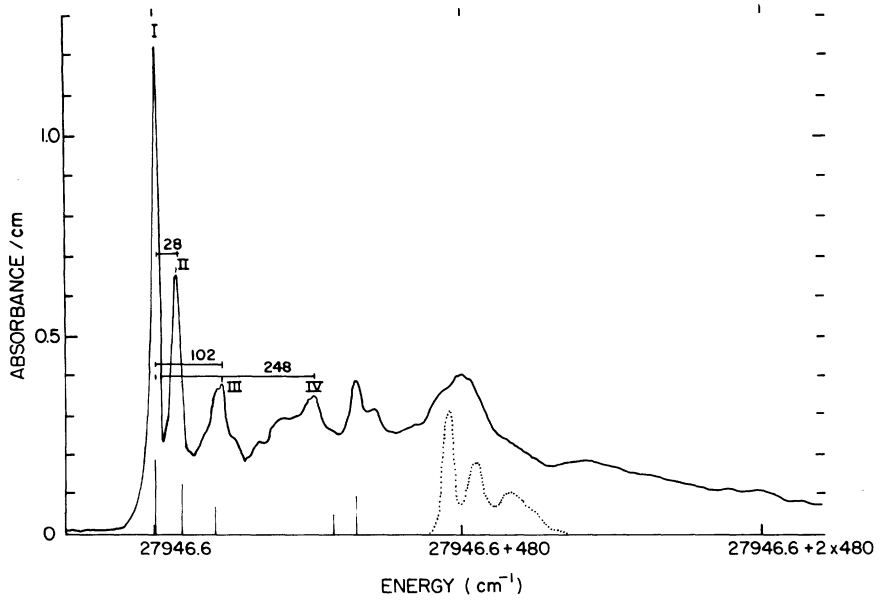

FIG. 14. Absorption spectrum of the $^4T_{2g}$(II) transition. The bars at the bottom indicate the calculated energies and relative intensities of the spin-wave sidebands for each of the twelve sublevels (only five have intensity) without the inclusion of a Jahn-Teller effect. The dotted band reproduces spin-wave sidebands I, II, and III, increased in energy by approximately 470 cm^{-1} and decreased in intensity by a factor of 0.2.

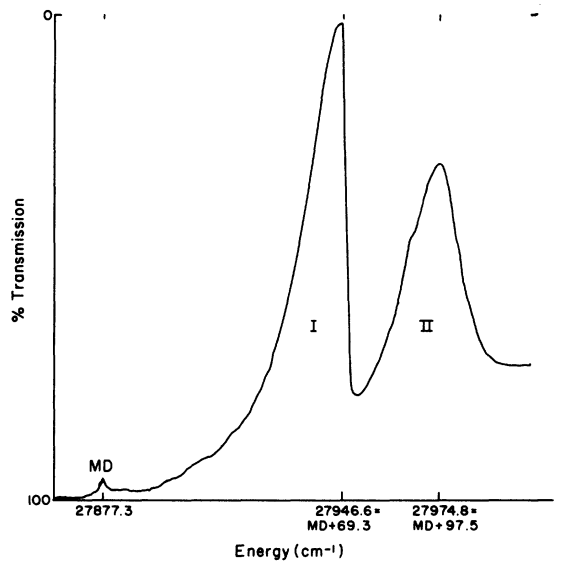

FIG. 15. Percent transmission tracing of the magnetic dipole (MD) and first two spin-wave sidebands (I and II) contained in the first 100-cm^{-1} region of $^4T_{1g}$(II).

feature in this region suggests it should be built upon the first, most intense, origin I, but it does not have the same polarization characteristics as I. Thus, since this peak does not behave like any of the three origins, there must be a new source of electric dipole activity in this region, either due to higher energy spin waves or odd-parity vibronic bands built upon the pure exciton transitions. The latter, however, can be eliminated by the temperature dependence given in Sec. V.

We also observe a broad intense band at 340 cm^{-1}, IV a, having the same polarization characteristics under stress as the 248-cm^{-1} band. This band should be the totally symmetric LA (at zone edge) now adding to this fourth-electric-dipole origin. It is superimposed on a region (300–350 cm^{-1}) which also shows two distinct peaks at 316 and 344 cm^{-1}, I b and II b, that reflect the polarization and energy shift of the first two spin-wave origins. They have been assigned in Sec. V D as the A_{1g} cluster excitation of LO_2. Between 400 and 450 cm^{-1} we find two more bands, I c and II c, which are seen to become more distinct with increasing [100] stress. These also have polarizations and energies reflecting the first two origins and correspond in energy to the zone edge values of LA + LO_2, the two most prominent one-quantum transitions in the low-energy region of the spectrum. Finally, the most intense structure in the entire transition, starting from about 470 cm^{-1}, I d, II d, and III d, reflects the energy shift and polarizations of the three (0-, 28-, and 102-cm^{-1}) origins and is the zone edge, LO_3, ~470-cm^{-1} mode.

In Fig. 17 we have indicated several sets of vibrational spacings, each built upon the previously identified electric-dipole origins. The sum of these accounts very well for all the observable structure and the polarization and energy shift behavior of the whole transition under stress, as seen in Fig. 16. Each set of vibrations indicated contains only energies which correlate well to A_{1g} and E_g cluster modes. Thus there is no large T_{2g} Jahn-Teller effect.

The σ-polarized spectrum of a crystal under [111] stress, shown at the top of Fig. 16 makes a vibrational analysis particularly simple, because the fourth and third spin-wave sidebands are missing, and the remaining structure is principally due to only the first and most intense origin. The prominent structure, labeled I a, I b, I d, are at

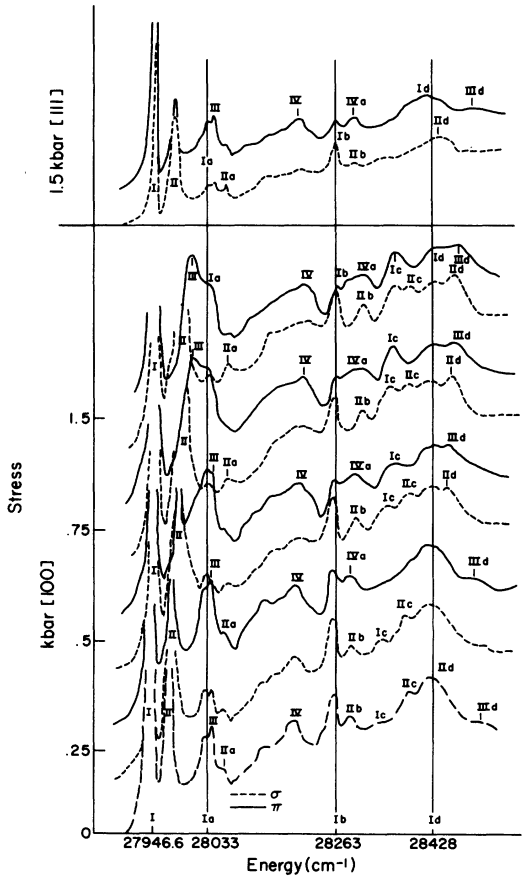

FIG. 16. Polarized stress response of the $^4T_{2g}$(II) transition. Microdensitometer tracings for stress in the [100] and [111] directions. The rather complicated polarization and energy shift effects are discussed in the text. The tracings are shifted to have the first spin-wave sideband (I) (at 27 946.6 cm^{-1} at 0 stress) coincide at all stress values.

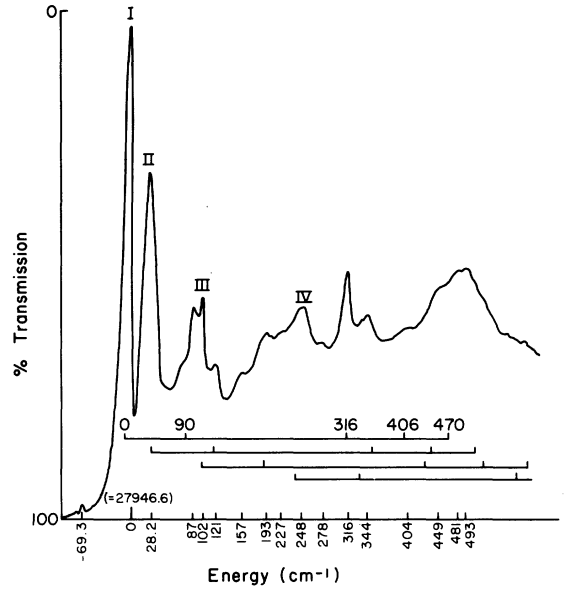

FIG. 17. Percent transmission tracing of the $^4T_{2g}$(II) transition with the energy measured relative to spin-wave sideband I. Four sets of associated (see text) vibrational structure are indicated, each having an identified spin-wave sideband as its origin.

the same energies as the peaks found for the $^4T_{1g}$(I) state. The only remaining differences between the spectra can be attributed to the bands built on the second origin of $^4T_{2g}$(II). This is further evidence that T_{2g} cluster contributions are not strong, and that our vibrational analyses shown in Figs. 2 and 17 are correct even in the cases where several spin-wave sideband origins are present.

The effect of tetragonal stress on the first three spin-wave sidebands of $^4T_{2g}$(II) is shown in Fig. 18 and plotted in Fig. 19. The lowest level increases in energy by 0.2 cm^{-1}/kbar, and the 28.2-cm^{-1} level shifts during spin reorientation and then decreases by 7.5 cm^{-1}/kbar. The sideband at 102 cm^{-1} undergoes a large spin-reorientation shift to lower energy so that it is now overlapped by the vibrations. The energy then decreases with increasing stress by about 4 cm^{-1}/kbar.

The three spin-wave-sideband origins also show three different responses to trigonal stress. These effects are illustrated in Fig. 20 and plotted in Fig. 21. The observed slopes are -3.8 cm^{-1}/kbar (for origin I), -1.3 cm^{-1}/kbar (for origin II), and -3 cm^{-1}/kbar (for origin III).

The axial spectrum in a magnetic field along the [100] or [111] direction is illustrated in Fig. 22 and the results are tabulated in the [110] spin-direction column of Table IX.

The spin-reorientation effects are collected in Table IX along with calculations of their magnitude to be discussed later. The stress response values are collected in Table XI along with other data, and a comparison of all the ^4T states shown there will be discussed later.

The $^4T_{2g}$(II) transition is the only one for which we find very different stress response among the first three origins (+0.2, −7.5, and −4.0 cm^{-1}/kbar). For $^4T_{1g}$(I) and $^4T_{1g}$(II) two levels had very similar slopes on the stress response diagrams.

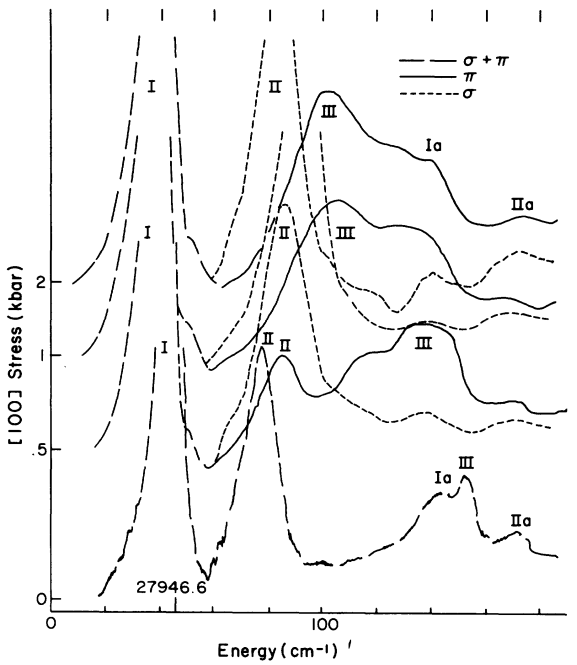

FIG. 18. Microdensitometer tracings of the effects of a [100] stress on the first 120-cm^{-1} region of the $^4T_{2g}$(II) transition.

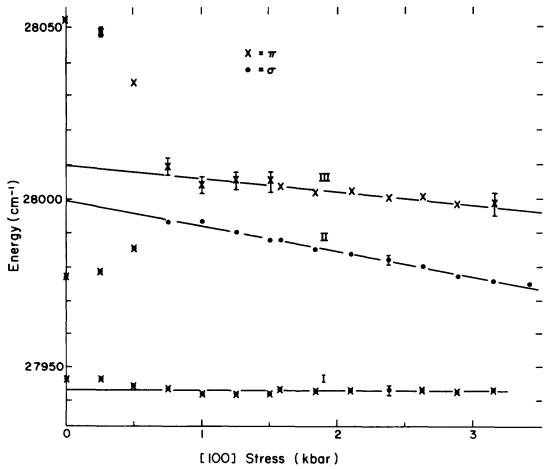

FIG. 19. Plot of the [100] stress response of the first three spin-wave sidebands of $^4T_{2g}$(II).

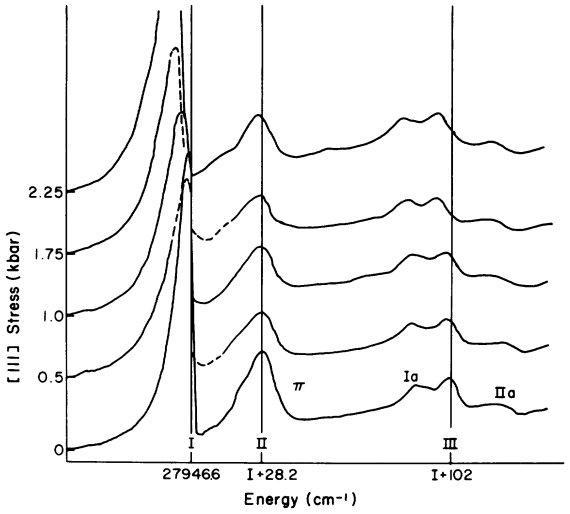

FIG. 20. Microdensitometer tracings of the effects of a [111] stress on the first 120-cm^{-1} region of the $^4T_{2g}$(II) transition. Only π polarization is shown because all the bands are partially π polarized.

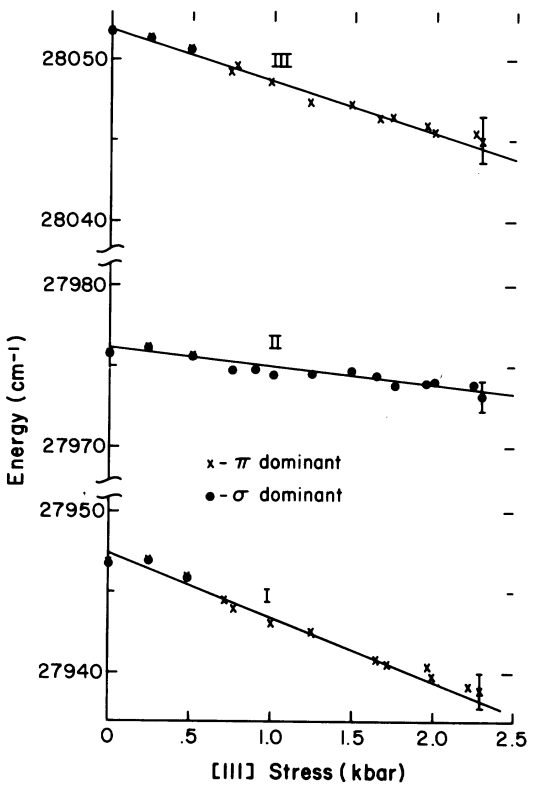

FIG. 21. Plot of the [111] stress response of the first three sidebands of $^4T_{2g}$(II).

This feature and the unusually large spin-reorientation effect will be explained in the following sections.

B. Energy-level calculations for $^4T_{2g}$(II)

1. Assumption of no Jahn-Teller effect

The large response to spin reorientation, and the differences of intensity and stress response among the sublevels of $^4T_{2g}$ compared to the other states show that the Jahn-Teller effect must be small. In this section we will present the results of calculations of the spectrum assuming it is zero.

Figure 14 shows the results of a calculation of the energies and intensities of the multiplet components assuming H_{ex} = 890 kG in the [111] direction and using the spin-orbit parameters of Table III, and assuming no Jahn-Teller distortion. There are five levels having significant intensity at 0, 38, 92, 288, and 316 cm^{-1}. The energies and intensities of the first three sidebands at 0, 28, and 102 cm^{-1} are fitted fairly well. Sideband IV at 248 cm^{-1} could be identified with one of the higher intense components of Fig. 14, but it is definitely lower than the computed value. Both the large splitting and the spread of intensity into the higher levels is consistent with the presence of a large spin-orbit interaction. As a result of this moderately good agreement between the calculated and observed spectrum, the Jahn-Teller effect must indeed be small.

The interval between the sidebands I and II increases by 27 cm^{-1} as the spin rotates from [111] to [100], while the I-III interval decreases by 32 cm^{-1}, as shown in Table IX. (Here we refer to the changes of the intervals with spin reorientation instead of the absolute values of the intervals because the latter depend on the sideband shape. The shape does not change with spin reorientation, so the changes of the intervals are independent of shape.)

The calculations give the correct qualitative behavior for the interval changes, but are quantitatively too low: the I-II interval increases by 13 cm^{-1} and the I-III interval decreases by 5 cm^{-1} according to the calculations.

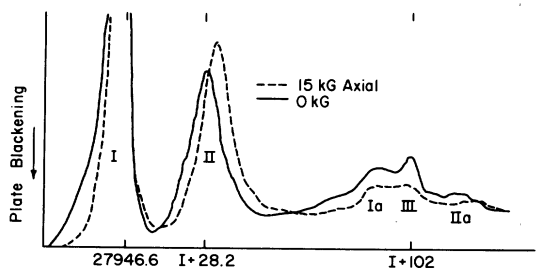

FIG. 22. Microdensitometer tracing of the axial spectrum in a [111] magnetic field of the first 120-cm^{-1} region of the $^4T_{2g}$(II) transition.

TABLE IX. Multiplet spacings in cm^{-1} for different spin directions for $^4T_{2g}$(II).

		Spin direction [111]	[110]	[100]
Experimental values	III	102	~90[a]	~70[a]
	II	28.2[b]	34.6[b]	55[b]
	I	0	0	0
Calculated[c] values	III	109	106	96.5
	II	38.5	42	65.5
	I	0	0	0

[a]Overlap with the vibrational sidebands makes accurate energy determination difficult.

[b]Measured from peak; zone edge should be 10 ± 3 cm^{-1} higher in energy.

[c]Calculated using one E_g quantum in Eqs. (7.1)–(7.3) with $\rho = -6.5$ cm^{-1}, $\kappa = 0.0$, $H_{ex} = 1100$ kG, $E_E = 40$ cm^{-1}.

Increasing the exchange field from 890 to 1100 kG has practically no effect on the spin reorientation response, although it increases the separation of the levels. We must therefore investigate the possibility that there is a small Jahn-Teller effect.

As mentioned earlier, the first three sidebands of $^4T_{2g}$(II) have different stress response, while for $^4T_{1g}$(I) and $^4T_{1g}$(II), two levels have the same response, and the other has minus twice this response. The latter behavior reflects the equivalence of the $|x\rangle$ and $|y\rangle$ partners with respect to a distortion along the z axis and it results from the reduction of the $\langle x|L_Y|z\rangle$ angular momentum matrix elements by the Jahn-Teller effect, and the $|x\rangle$, $|y\rangle$, and $|z\rangle$ designation of the substates becomes appropriate.

For the $^4T_{2g}$(II) state, however, there is large spin-orbit mixing of the $|x\rangle$, $|y\rangle$, and $|z\rangle$ partners. Since the lowest level contains only $|x+iy\rangle$ independent of the magnitude of the Jahn-Teller effect, we can substitute the experimental value of the stress response for this level 0.2 cm^{-1}/kbar for [100] stress to obtain the matrix element for the $|x\rangle$ (or $|y\rangle$) stress response. This matrix element can then be used in conjunction with the observed stress response and wave function of the higher levels to extract the $|z\rangle$ stress response (for, say, the [100] spin direction). This quantity $\langle z|H(100)|z\rangle$ should be the same in any level if we have the correct wave functions for each level. We find, however, that for level II, $\langle z|H(100)|z\rangle = -12.5$ and for III it is -6.7 cm^{-1}/kbar. Therefore, the wave functions must not be strictly correct. Variation of the exchange field does not improve matters so we have another reason to consider a nonzero Jahn-Teller effect.

2. *Inclusion of the Jahn-Teller effect*

Although the theoretical explanation of the spectrum is fairly good, several discrepancies noted in Sec. VII B 1 suggest that the inclusion of vibronic effects should be investigated.

The results of a Ham-type calculation for an E_g Jahn-Teller distortion with $H_{ex} = 890$ kG in the [111] direction are shown in Fig. 23. In this calculation, second-order vibronic terms are found to be important and so it may be necessary to include higher-order corrections for more accuracy. Therefore, a more complete calculation was done whose results are also shown in the low-energy region of Fig. 23.

In this calculation we have attempted to solve the electronic and vibronic Hamiltonians simultaneously. Due to the complexity of the spin-orbit–plus–exchange wave functions, however, we only include one E_g vibrational quantum explicitly in a 72×72 spin-orbit–plus–exchange matrix [formulated in terms of a real orbital basis $(i, j = \xi, \eta, \zeta)$]. Ham *et al.*[32] found three quanta to give fairly good convergence up to $E_E = 0.6\hbar\omega_E$. It is a reasonable expectation for our case that one quantum will reproduce the dominant effects.

The Jahn-Teller distortion was therefore expressed by including a vibrational overlap integral between displaced doubly degenerate (m_i, n_i) har-

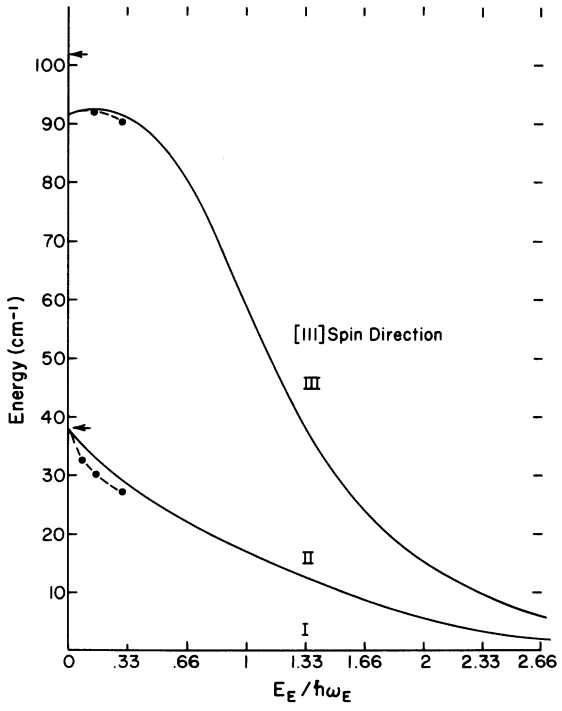

FIG. 23. [111] Ham effect diagram for $^4T_{2g}$(II) using $H_{ex} = 890$ kG. The dotted lines at low energies give the results of a calculation which explicitly includes one quantum of a 328-cm^{-1} vibration. The arrows on the ordinate give the observed energy spacings.

monic-oscillator wave functions belonging to different electronic partners i, j. The terms of Hamiltonian (3.1) which were included are

$$\langle i, M_s, m_i, n_i | \mathcal{H}'_{\text{vib}} | j, M'_s, m'_j, n'_j \rangle = \hbar\omega_E (m+n)\delta(ij)\delta(mm')\delta(nn')\delta(M_s M'_s), \quad (7.1)$$

$$\langle i, M_s, m_i, n_i | \mathcal{H}_{\text{so}} | j, M'_s, m'_j, n'_j \rangle = \langle i, M_s | \mathcal{H}_{\text{so}} | j, M'_s \rangle \langle m_i | m'_j \rangle \langle n_i | n'_j \rangle, \quad (7.2)$$

and

$$\langle i, M_s, m_i, n_i | \mathcal{H}_{\text{ex}} | j, M'_s, m'_i, n'_j \rangle = \langle M_s | \mathcal{H}_{\text{ex}} | M'_s \rangle \delta(ij)\delta(mm')\delta(nn'), \quad (7.3)$$

with $\mathcal{H}'_{\text{vib}}$ ($=\mathcal{H}_{\text{vib}}$ if $V_A = V_E = V_T = 0$ and $\gamma = \theta$, ϵ) being the undistorted nuclear Hamiltonian for an E_g vibrational mode. The overlap integrals appearing in Eq. (7.2) have previously been calculated by Sturge and Guggenheim.[33]

The results of the calculations show that the 38-cm^{-1} interval is fitted by $E_E = 0$, but that no value of E_E will fit the 102-cm^{-1} interval. Therefore, we increased the exchange field to 1100 kG and repeated the more elaborate calculation for three spin directions. The results are shown in Fig. 24. The most significant result is that the spin-reorientation energies are increased by including a small Jahn-Teller effect. A value of $E_E = 40$ cm^{-1} gives the best fit to the spin-reorientation changes of the first interval. The calculated spin-reorientation effect for the interval I-III also increases with E_E, but not by nearly enough. We will return to this problem later.

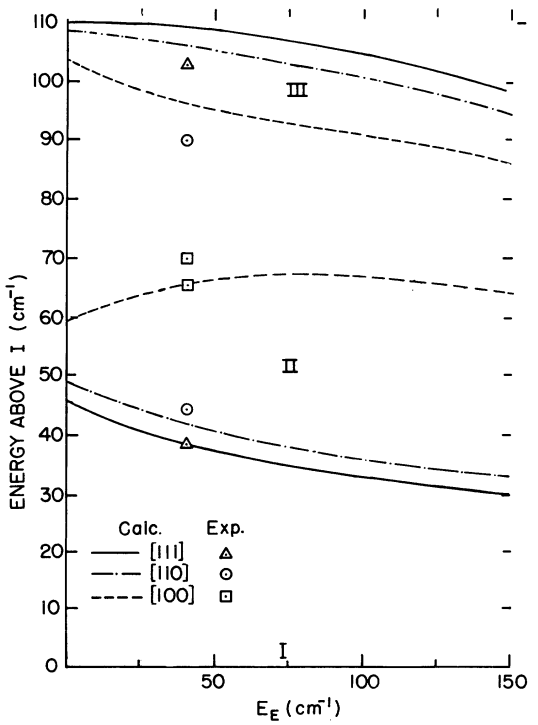

FIG. 24. Results of using $H_{ex} = 1100$ kG and including one vibrational quantum explicitly in the Jahn-Teller calculation for $^4T_{2g}$(II) for three directions of H_{ex}. The points show the intervals between the three sidebands for the three orientations of H_{ex}, and are plotted at the value of E_E (using $\hbar\omega_E = 328$ cm^{-1}), which best fits the calculation.

The physical reason for the Jahn-Teller enhancement of the spin-reorientation effect can be seen in the second-order in-state vibronic terms in Ham's equation (2.24) of Ref. 11. For small Jahn-Teller energies and large spin-orbit parameters, the term $K_2(L_x^2 S_x^2 + L_y^2 S_y^2 + L_z^2 S_z^2)$ becomes important, and since it does not commute with H_{ex}, it gives rise to spin anisotropy.

The small Jahn-Teller distortion has very little effect on the intensities, but lowers the upper levels (at 288 and 316 cm^{-1} for $H_{ex} = 890$ kG referred to in Sec. VII B 1) to 245 and 255 cm^{-1}. These agree more closely with band IV at 248 cm^{-1}.

We now show how the inclusion of a small Jahn-Teller effect can resolve the problem described in Sec. VII B 1 of the different values of $\langle z | H(100) | z \rangle$ in the three lowest sublevels. We use the facts that $\langle x | H(100) | x \rangle = \langle y | H(100) | y \rangle = 0.2$ cm^{-1}/kbar and that the wave functions of the three states are a function of E_E. The change of $\langle z | H(100) | z \rangle$ with E_E is shown for levels II and III in Fig. 25. The curves cross at $E_E = 165$ cm^{-1}. Thus, we find a value $\langle z | H(100) | z \rangle = -9.8$ cm^{-1}/kbar, which is the same in levels II and III.

The value of $E_E = 165$ cm^{-1} just obtained is four times the value obtained from the spin reorientation, but the difference between the two calculations is that the wave function of level III must be used here, and not in the first calculation. In the first calculation the spin-reorientation shift of level III could not be accounted for. Both calculations show that we do not know the wave function of level III, and that variations of the exchange field and Jahn-Teller energy have not helped enough. A possible explanation for the difficulty is that level III overlaps the first phonon sideband of levels I and II (see Fig. 2) and therefore may be vibronically coupled to those levels. As shown in Sec. V and Table VII, the LA(X) phonons have E_g character at the Mn site. Levels I and III are of the proper symmetry to be coupled by a cluster vibration of $E\epsilon$ type. Therefore we cannot expect a Jahn-Teller calculation based on a single cluster mode at 328 cm^{-1} to do justice to level III, since this level sees the distinct phonon nature of the lattice. Sturge has considered a similar case.[33] For the above reasons we feel that the value of 40 cm^{-1} for E_E is more realistic, as further investigation will show.

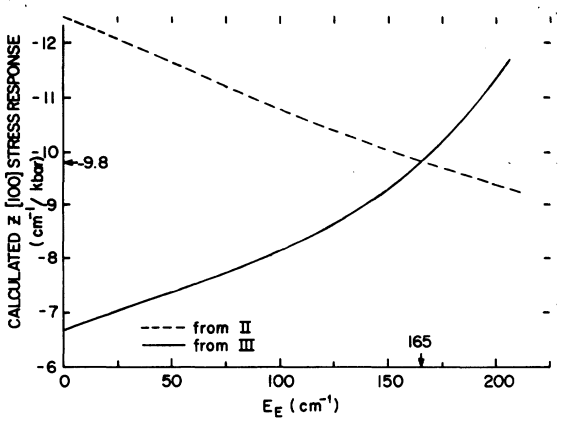

FIG. 25. $\langle Z|$ partner stress response calculated from the wavefunctions modified by the Jahn-Teller effect of sublevels II and III. A consistent value of -9.8 cm^{-1} kbar is obtained with $E_E = 165$ cm^{-1}.

3. *Jahn-Teller energy from the stress data*

In Sec. VII B 1 we showed how to find the matrix elements of the stress response from the experimental stress response, and in part 2 we showed that a Jahn-Teller energy had to be present in order to obtain a consistent value of $\langle z|H(100)|z\rangle$ for levels II and III. The tetragonal splitting, $\langle z|H(100)|z\rangle - \langle x|H(100)|x\rangle$, was found to be -10 cm^{-1}/kbar.

This value corresponds to a force [using Eqs. (3.9), (3.10) and (3.5)] $V_E = -0.46\times10^{-4}$ dyn, a displacement $Q_\theta = -0.05$ Å and an E_g Jahn-Teller energy of 58 cm^{-1}, in fair agreement with the value obtained from the one-quantum calculation, Fig. 24.

The average, or hydrostatic shift of the bands is -3.8 cm^{-1}/kbar. This value corresponds [using Eqs. (3.9), (3.10), and (3.4)] to $V_A = -0.89\times10^{-4}$ dyn, $Q_a = -0.05$ Å, and $E_A = 110$ cm^{-1}. Then using Eq. (4.4b), these values of V_A and V_E can be combined to give $S_{LO_3} = 0.2$. Sidebands I, II, and III reduced by this factor are plotted in the 470-cm^{-1} region of Fig. 15. Their magnitude is in good agreement with the appearance of the spectrum in this region.

A value of the hydrostatic shift can also be obtained by averaging the $|x\rangle$, $|y\rangle$, and $|z\rangle$ tetragonal stress matrix elements derived in Sec. VII B 2. This treatment of the experimental data gives nearly the same value as above, -3.3 cm^{-1}/kbar.

Treated in a similar fashion, the trigonal-stress data, Fig. 22, give a hydrostatic shift of -2.7 cm^{-1}/kbar and a trigonal splitting of 3.3 cm^{-1}/kbar, the Z partner going up in energy. This is close to the magnitude we found experimentally for $^4T_{1g}$(II). However, the trigonal splitting of $^4T_{1g}$(II) had been quenched by a sizable E_g Jahn-Teller effect. The small $E_E = 58$ cm^{-1} found for $^4T_{2g}$(II) produces only a small quenching of the [111] stress response. Using only the first-order quenching factor $\exp(-\frac{3}{2}\frac{58}{267}) = 0.74$, we obtain an unquenched trigonal splitting of about 4.5 cm^{-1}/kbar. This value corresponds to a T_{2g} Jahn-Teller energy of 8.3 cm^{-1} which is too small to have a noticeable effect on the spectrum.

To summarize, for this transition only we have found evidence for a significant spin-orbit interaction. This evidence includes the large separation of unperturbed origins, the large intensity differences among these origins and their very different stress responses. We did, however, need to include some Jahn-Teller effect in order quantitatively to fit the origins and their stress responses, and to increase the calculated spin reorientation effects to agree with the observed large shifts. Since the results are in a region of a larger spin-orbit interaction and smaller Jahn-Teller effect, diagonalization of the complete electronic plus vibronic Hamiltonian is necessary for an accurate treatment. This still fails for the electronic level contained in the vibrational region, since the cluster-mode approximation is no longer valid for this level.

VIII. $^4T_{2g}$(I)

The spectrum of the $^4T_{2g}$(I) transition is presented in Fig. 26(a). The only structure observable even under high resolution is a broad nonharmonic progression with intervals between maxima of about 430, 410, and 390 cm^{-1}. The lack of sharp struc-

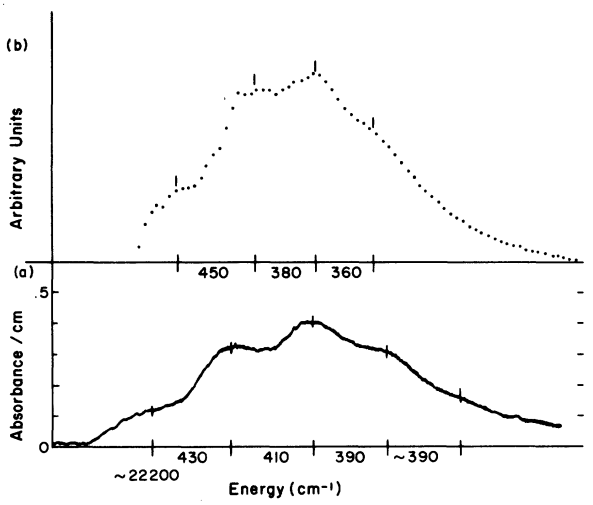

FIG. 26. (a) Absorption spectrum of the $^4T_{1g}$(I) transition. (b) A curve synthesized from a normalized sum of three $^4T_{1g}$(I) curves (Fig. 5) separated as calculated using $E_E/\hbar\omega = 0.5$. Approximate peak separations for both curves are indicated.

ture precludes the approaches used in the studies of the other transitions. We can, however, use the insights which we have obtained from the studies of the other states to get a general idea of what must be occurring in this transition. We should thus be able to account for the lack of sharp structure, the overall band shape of Fig. 26(a), and the less than 470-cm^{-1} intervals of the prominent vibration.

The logical conditions which would both eliminate the sharp structure and account for the over-all line shape are to have several electric-dipole origins, spaced fairly far apart as in $^4T_{2g}$(II) (Fig. 17), each having a phonon sideband with a large Franck-Condon factor built onto it, as in Fig. 5 for $^4T_{1g}$(I).

The combination of distortions which can produce these conditions is a fairly small E_g (and T_{2g}) distortion, which causes only a small quenching of the spin-orbit splitting, and a large A_{1g} distortion the major factor in producing the large phonon sideband.

Table X gives the calculated spin-orbit–plus–exchange energies of the sublevels having spin-wave intensity for different values of the Jahn-Teller quenching. The $E_E = 0$ value shows these lowest three levels to have an over-all separation of 110 cm^{-1} without a Jahn-Teller quenching, about twice the 58-cm^{-1} calculated for $^4T_{1g}$(I). Even though these multiplet levels have almost the same spin-orbit parameter, the change in sign of λ for $^4T_{2g}$(I) is significant (see Table III). Changing the sign inverts the first-order spin-orbit splitting in Fig. 1, leaving the sixfold degenerate level (which contains one pure $M_s = -\frac{3}{2}$ sublevel) highest in energy. When coupled with the exchange field, this leads to the large energy splitting. Table X also shows that the spin-orbit splitting of the $M_s = -\frac{3}{2}$ multiplet is sizable for Jahn-Teller energies of $E_E/\hbar\omega_E = 1.0$ and below. The range of $E_E/\hbar\omega_E = 0.2$–0.8 would produce the magnitude of splitting needed to give overlap of the sidebands without allowing them to converge into one origin, as happened in $^4T_{1g}$(I). Using an intermediate value of $E_E/\hbar\omega_E = 0.5$, we obtain $V_E = -7.2\times10^{-5}$ dyn and $Q_\theta = -0.079$ Å. The inward direction of distortion along the z axis would be obtained from the crystal-field stress expression in Table XII for any reasonable values of the second- and fourth-power terms.

TABLE X. Calculated spin-orbit–plus–exchange splittings for $^4T_{2g}$(I).

	$E_E/\hbar\omega_E$ = 0		0.33		1.0	
	Energy (cm^{-1})	Intensity	Energy (cm^{-1})	Intensity	Energy (cm^{-1})	Intensity
III	110.6	1	66.3	1	23.4	1
II	47.1	0.89	33.3	0.94	12.7	1
I	0	0.91	0	0.95	0	1

We have also included in Fig. 26(b) a band shape which has been derived from a superposition of three complete $^4T_{1g}$(I) transitions. Each transition originates from single sideband origins which are now separated by the energies calculated on the basis of a 164-cm^{-1} E_g Jahn-Teller quenching energy.

It is reasonable to use a superposition of $^4T_{1g}$(I) band shapes in the present case because in each case, the A_{1g} force is dominant. The separation of the sidebands is comparable to their width so that only a single broad origin is observed. The superposition also accounts for the effective decrease in vibrational spacings. (The derived curve gives 450, 380, and 360 cm^{-1}.) The small differences between the calculated and experimental curves could have been removed had we varied the parameters.

Using $S_{LO_3} = 1.3$, the $^4T_{1g}$(I) Franck-Condon factor, the approximate $V_E = -8.9\times10^{-5}$ dyn and the fact that the A_{1g} distortion direction is necessarily inward (from the stress expression in Table XII) we calculate, from Eq. (5.4b), $V_A = -2.4\times10^{-4}$ dyn/cm, $Q_A = -0.134$ Å, and $E_A = 815$ cm^{-1}.

IX. COMPARISON OF THE JAHN-TELLER EFFECTS IN THE FOUR T STATES

Table XI summarizes the properties we have found for the four T states. The Jahn-Teller energy E_E and the energy of the symmetric displacement E_A change by an order of magnitude within this group of states as shown in columns 5 and 10 of Table XI. Similarly, the displacements which are illustrated in Fig. 27 and recorded in columns 4, 9, and 16 differ greatly from one state to another.

One obvious spectral consequence of the Jahn-Teller effect is the decrease of the spin-orbit multiplet width with increasing E_{JT}. By comparing the spectra of the states in the order shown in Table XI [omitting $^4T_{2g}$(I)], we have found that the splitting increases from 6 to 29 to 102 cm^{-1} for the lowest exchange triplet, while E_E goes from 458 to 143 to 58. Associated with this change is an increase in the spread of spin-wave sideband intensity over higher multiplet components. In T_1(I) only the lowest three sidebands are observable, and all have the same intensity; in T_1(II) the third sideband is weakened but higher ones cannot be seen, and in T_2(II) the first three have different intensities and higher ones are fairly strong.

The change of energy vs stress in the lowest exchange triplet shows two equal slopes and one different one for $^4T_1$(I) having large E_E, three very different slopes for $^4T_2$(II) having the smallest E_E, and two with similar but unequal slopes, and one

TABLE XI. Summary of results[a] for the four orbital triplet states.

	Hydroshift (cm^{-1}/kbar)	V_A (10^{-4} dyn)	Q_A (Å)	E_A (cm^{-1})	u (10^3 cm^{-1})	[100] split (cm^{-1}/kbar)	V_E (10^{-4} dyn)	Q_θ (Å)	E_E (cm^{-1})	u (10^3 cm^{-1})	v (10^3 cm^{-1})	S_{LO_1}	[111] split (cm^{-1}/kbar)	V_T (10^{-4} dyn)	$Q_{T_2\chi}$ $[Q_\xi Q_\eta Q_\zeta]$ (Å)	E_T (cm^{-1})	v (10^3 cm^{-1})
$^4T_{1g}$(I)	−9.5	−2.23	−0.125	703	40	28	1.3	0.140	458	33.5	b	1.3	<0.4	0	0	0	c
$^4T_{1g}$(II)	2.7	0.7	0.040	70	16.5	−19[d]	−0.73	−0.095	143	29.5	b	0.25	−8.5[d]	−0.12	−0.04	22	12[e]
$^4T_{2g}$(I)[f]	...	−2.4	−0.13	815	c	c	−0.72	−0.079	144	g		1.3	c	c	c	c	c
$^4T_{2g}$(II)	−3.8	−0.89	−0.05	111	59.5	−10[d]	−0.46	−0.050	58	g	23	0.2	4[d]	0.07	0.02	8.3	14[e]

[a]Obtained from Secs. V–VIII.
[b]Not appropriate.
[c]Could not be obtained by experiment due to lack of structure.
[d]Corrected to unquenched value (see text).
[e]Assumes $u = 23.4 \times 10^3$ cm^{-1}.
[f]Approximate values.
[g]Could not be independently obtained.

very different for $^4T_1$(II) with intermediate E_E. Also, the magnitude of the stress response increases with the Jahn-Teller energy.

The spin-reorientation effects are largest when the Jahn-Teller effects are small but not zero. When E_{JT} is large, only out-of-state second-order spin-orbit terms are left to produce a small residual spin reorientation effect, as seen in $^4T_1$(I). With zero E_{JT}, there would again be only these small reorientation energies, as is found for the ^4A, ^4E states, as mentioned in Ref. 2.

Finally, the phonon sideband was found useful in signalling the presence of the T_{2g} type of Jahn-Teller effect, but for the E_g type it was not as useful because of the difficulty of separating A_{1g}- and E_g-type contributions.

The directions of the distortions shown in Fig. 27 were obtained entirely from the sense of the stress effects. We now show that these directions can be explained qualitatively by using the wave functions given in Table I and the configurational coefficients in Table II. First, the change in average bond length, caused by the hydrostatic shifts, is determined by $\alpha^2 - \gamma^2$ of Table II, since this quantity tells whether the amount of antibonding e orbital has increased or decreased upon electronic excitation. Thus the signs of $\alpha^2 - \gamma^2$ in Table II are opposite from those of Q_A in Table XI. Second,

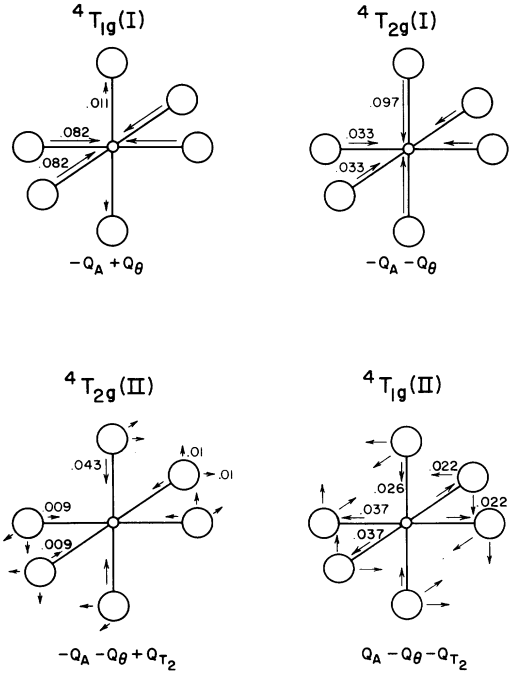

FIG. 27. Geometries of the orbital triplet excited states of Mn^{++} in $RbMnF_3$. The numbers give the magnitudes of the distortions in Å in the directions indicated by the arrows.

the sign of the tetragonal distortion is determined by whether the occupation of ϵ or of θ is increased by the transition. For $^4T_1$(I), the transition is principally $\epsilon \rightarrow \zeta$, which increases the antibonding effect in the ζ direction resulting in $Q_\theta > 0$. For $^4T_2$(II), since $\alpha^2 > \gamma^2$, $\theta \rightarrow \zeta$ predominates and the opposite change in Q_θ results. For $^4T_1$(II), $\gamma^2 > \alpha^2$ and $\zeta \rightarrow \epsilon$ predominates and again $Q_\theta < 0$. All of these results agree with those of Table XI.

X. APPLICABILITY OF THE CRYSTAL-FIELD MODEL

Since we have a cubic, highly ionic system containing $3d$ electrons, we should investigate the applicability of the crystal field model to our data, and then see if it can be used to make predictions about the Jahn-Teller effect in other systems. To do this, we first define the static coupling constants V_r' in terms of the model.

We depend on only two properties of the crystal-field model: the independence of the bonds (additivity) and the separability of radial and angular factors. Thus the form of the crystal-field potential is

$$V^c = \sum_b V_b = \sum_b \sum_1 f_1(r, R_b) g_1(\theta_b), \tag{10.1}$$

where b sums over the nearest-neighbor bonds, f depends only on bond length R_b and electron radius vector r, and $g_1(\theta_b)$ is a function only of the angle θ_b made by the radius vector of the electron with the bonds b. The index 1 results from the expansion in spherical harmonics. The strain potentials are

$$\frac{\partial V^c}{\partial Q_r} = \sum_b C_b^r \frac{\partial V_b}{\partial X_b^r}, \tag{10.2}$$

where the C_b^r describe the relative displacements of the ligands in normal coordinate Q_r [from Eq. (2.2)] and the X_b^r are the displacements in Q_r.

Now we make further assumptions by introducing the point charge model for V_b and obtain formulas such as

$$\frac{\partial V^c}{\partial Q_\theta} = \left(\frac{3e}{R^3}(2z^2 - x^2 - y^2) + \frac{5}{4}\frac{5e}{R^5}(z^4 + 6x^2y^2 - \tfrac{3}{5})\right)(S_{11} - S_{12})P. \tag{10.3}$$

A matrix element of this potential can be written

$$\langle T_1 Z \left| \frac{\partial V^c}{\partial Q_\theta} \right| T_1 Z \rangle = \frac{4}{9}(\alpha^2 - \gamma^2)\frac{5}{4}\frac{5e^2\langle r^4\rangle}{R^5}(S_{11} - S_{12})P, \tag{10.4}$$

where the first factor depends on the $3d$ wave functions, the second on the type of strain, the third on the details of the point charge model and the fourth on the type of stress. The third factor is the one most difficult to evaluate *a priori* and it must be obtained from experiment. In Refs. 1 and 2, we used

$$e\langle r^4\rangle/R^5 = 6Dq, \tag{10.5}$$

where Dq was obtained by fitting the six lowest bands of the electronic spectrum. The factor 5, the exponent of R, is specified by the point-charge model. The measured stress response should be proportional to the product of all factors in Eq. (10.4). If we believe the two major premises of the crystal-field model, the stress response data may be used to evaluate the third factor, and the results may be compared to the value obtained from Eq. (10.5).

To carry out this program we write the expressions for the static coupling constants V_r' of Eq. (3.1d) as follows:

$$\begin{aligned}
&V_A'(T_1 \text{ and } T_2) = 10(\alpha^2 - \gamma^2)\tfrac{1}{6}u,\\
&V_E'(T_1) = \tfrac{4}{9}(\alpha^2 - \gamma^2)\tfrac{5}{4}v,\\
&V_E'(T_2) = -8(\alpha^2 - \gamma^2)v + \tfrac{4}{63}(\alpha^2 - \gamma^2)\tfrac{5}{4}u,\\
&V_{T_2}'(T_1) = \tfrac{1}{14}[(-\alpha^2 + \gamma^2) + (2\sqrt{2})(\alpha\beta + \beta\gamma)]2v\\
&\qquad + \tfrac{6}{14}[(\alpha^2 - \gamma^2) + (3/\sqrt{2})(\alpha\beta - \beta\gamma)]\tfrac{1}{2}u,\\
&V_{T_2}'(T_2) = \tfrac{1}{14}[(-\alpha^2 + \gamma^2) + (2\sqrt{2}/\sqrt{3})(\alpha\beta + \beta\gamma)]2v\\
&\qquad + \tfrac{6}{14}[(\alpha^2 - \gamma^2) + (\sqrt{3}/\sqrt{2})(\alpha\beta + \beta\gamma)]\tfrac{1}{2}u,
\end{aligned} \tag{10.6}$$

where $u = 5e^2\langle r^4\rangle/R^5$ and $v = 3e^2\langle r^2\rangle/R^3$.

By the use of Eqs. (3.9), Eqs. (10.6) can be used to give the various types of stress response and these are shown in Table XII, where they are expressed in terms of the parameters u and v. The values of u and v can then be found by equating the appropriate expression of Table XII to the experimental stress response in Table XI. The values of u and v so obtained are collected in Table XI. For comparison, the value of u obtained from the spectroscopic Dq is $u(\text{spect}) = 30Dq = 23.4 \times 10^3$ cm^{-1}.

The u values in columns 6 and 11 of Table XI are not constant as they should be for a crystal-field model, and are larger than 23.4×10^3 cm^{-1} as the point-charge assumption requires. For the T_1 states whose stress response depends mostly on u, the values average about 30×10^3 cm^{-1}.

The great variability of the u values taken from the hydrostatic shifts (column 6, Table XI) is probably caused by the fact that the measured shift is a small change in an excitation energy of (20–30) $\times 10^3$ cm^{-1}, and these energies depend on the electrostatic parameters B and C of the crystal-field model as well as on u. We assumed that only the crystal field parameter changed with stress in writing the formulas (10.6) and Table XII, but this is not strictly correct.

An experimental correction can be introduced by using the stress dependence of $^4A_1$ or ^4E(I) at about 25 000 cm^{-1}. The energies of these states are independent of Dq, and their dependence on B and C is similar to that of most of the states we are dealing

TABLE XII. Crystal-field expressions for stress response (u, v in units of 10^3 cm^{-1}).

	Hydrostatic shift	Tetragonal splitting	Trigonal splitting
$^4T_1$(I)	$-0.24u$	$0.912u$	$0.185u-0.193v$
$^4T_1$(II)	$0.166u$	$-0.65u$	$-0.232u-0.263v$
$^4T_2$(I)	$-0.134u$	$0.074u-1.07v$	$0.041u-0.403v$
$^4T_2$(II)	$-0.062u$	$0.035u-0.5v$	$0.095u+0.13v$

with. The hydrostatic shift of $^4A_1$, ^4E is about -1.5 cm^{-1}/kbar[34] and when this is subtracted from 9.5 cm^{-1}/kbar, the hydrostatic shift of $^4T_1$(I), the value of u obtained is 34×10^3 cm^{-1} within error limits of the value 33.5×10^3 cm^{-1} obtained from the tetragonal splitting of $^4T_1$(I). The $^4T_1$(II) state also has almost the same B, C dependence as $^4A_1$, and when -1.5 cm^{-1}/kbar is subtracted from 2.7 cm^{-1}/kbar, a value $u=25\times10^3$ cm^{-1} is obtained, again in the same region as the value obtained from the tetragonal stress response. For $^4T_2$(II) the B, C dependence is somewhat less than for $^4A_1$, but the same correction should be reasonable, and in fact gives a corrected hydrostatic shift of -2.3 cm^{-1}/kbar and a value $u=37\times10^3$ cm^{-1}. The u parameter cannot be obtained from the tetragonal splitting of $^4T_2$(II), but the value 37×10^3 cm^{-1} is close to the corrected values for the other states. The average of the three corrected u values from hydrostatic shift is 32×10^3 cm^{-1}, while the average of the two tetragonal values is 31.5×10^3 cm^{-1}. These numbers suggest that within the error bounds of the stress measurements, a single value of u applies to all states for either hydrostatic or tetragonal stress.

The values of v, not usually obtainable in experiments with transition metal ions, are not very different from the u values. The two values obtained from trigonal splitting are considerably smaller than the value obtained from tetragonal splitting, but only the latter comes from a formula in which the splitting depends almost entirely on v. The other v values are very sensitive to the u value chosen.

The crystal-field model does give the correct signs of the trigonal splitting of the T_1(II) and T_2(II) states. In the formulas of Table XII the coefficients of u and v for the trigonal splitting have the same sign, and as u and v are necessarily positive, the sign of the splitting is unambiguously predicted. These signs could not be predicted by the qualitative arguments at the end of Sec. IX.

From the comparisons of the u and v parameters we have made, we see that the crystal-field model is crude, but not badly wrong. It is not good enough to be used to analyze our data, but could be used to estimate Jahn-Teller effects in new systems where measurements have not been made. Our data suggest that a simple and reasonable approximation is to take

$$e^2\langle r^2\rangle/R^3 = e^2\langle r^4\rangle/R^5 = 6Dq\,, \tag{10.7}$$

where Dq is obtained by fitting spectra in the usual way. The stress responses using this approximation are compared with the observed ones in Table XIII. All the signs are correct, and the magnitudes are within 50% except for the hydrostatic shifts (but the corrected shifts agree well). In many cases, Eq. (10.7) will be an acceptable approximation. Note that the observed splittings quoted in Table XIII are the same as those of Table XI, and have been corrected for Jahn-Teller quenching in several cases.

XI. CONCLUSIONS

$RbMnF_3$ is a nearly ideal system for a study in depth of its properties, as the abundance of research papers on this material indicates. Our research on the Jahn-Teller effect has depended on these other studies. More than anything else, we depended on the accurate compliance constants of Melcher and Bolef.[35] In a pure cubic material the compliance constants give the actual displacements of the atoms of interest, enabling us to eliminate the uncertainty which arises in the case of impurity systems. All other systems in which the Jahn-Teller effect in excited states has been studied were defect or impurity systems. We have therefore been able to obtain values of the Jahn-Teller energy and the associated atomic displacements.

Although the magnetic order could have been a complication, the low anisotropy and well-studied spin-reorientation behavior[17] became an advantage when we understood their spectral consequences.[2] Although we used the ground-state exchange field for most of the analysis, in the $^4T_2$(II) state there was evidence that a higher value was more appropriate. There is evidence in this state for different amounts of exciton-magnon binding in different exciton states, as shown by differences in spin-wave sideband shapes.

Our knowledge of the distortions in the excited states has led to fairly complete interpretation of the spectral structure. We have found that even small values of E_{JT} have appreciable spectral effects. Therefore we believe that multiplet interpretations on other systems must include such effects before they can be considered accurate. We found the T_2 type of Jahn-Teller distortion in a

TABLE XIII. Comparison of approximate crystal-field calculations [Eq. (10.7)] to observed stress response (in cm^{-1}/kbar).

	Hydro. calc	Shift obs	Te trag. calc	Split obs	Trig. calc	Split obs
$^4T_1$(I)	-5.6	-9.5	21.3	28	1.62	0
$^4T_1$(II)	3.92	2.7	-15.1	-19	-9.1	-8.5
$^4T_2$(I)	-3.14	···	-13.2	···	-4.7	···
$^4T_2$(II)	-1.46	-3.8	-6.2	-10	4.0	4

case where the E type was small, and showed that it had a significant effect on the phonon sideband.

Our results should be directly applicable to other Mn compounds, as well as to other transition metal compounds. For example, MnF_2 might now be treated accurately with the help of the reduction factors of $RbMnF_3$, and the static distortions could be studied independently of the dynamic ones. The semiquantitative description of the Jahn-Teller effect obtained through the crystal-field model should be useful for understanding systems where accurate measurements have not been made.

It would be interesting to have neutron-inelastic-scattering data for $RbMnF_3$ from which the phonon frequency distribution and wave functions could be obtained, and compared to our phonon sideband data. These results could be used to give accurate lattice force constants and coupling constants and finally an effective reduction factor independent of the cluster approximation.

Note added in proof. A slight numerical error in the value of the E-cluster frequency was discovered in reading the proof. This has been corrected in text and tables, but Fig. 27 contains the error and is not consistent with Table XI. The differences, however, are less than the experimental error of perhaps 20% arising from the experimental measurements, and indeterminate errors arising from the approximations used in the interpretation.

---

†Work supported by the National Science Foundation and by the Office of Naval Research under Contract No. N00014-67-A-0151-0012.

*Present address: Kemisk Laboratorium IV, Universitetsparken 5, Copenhagen, Denmark.

[1]M.-Y. Chen, D. S. McClure, and E. I. Solomon, Phys. Rev. B 6, 1690 (1972).

[2]E. I. Solomon and D. S. McClure, Phys. Rev. B 6, 1697 (1972).

[3]J. Ferguson, Australian J. Chem. 21, 307 (1968).

[4]We wish to thank Dr. D. D. Sell for giving us these samples of $RbMnF_3$.

[5]Y. Tanabe and S. Sugano, J. Phys. Soc. Jap. 9, 753 (1954).

[6]A. Mehra and P. Venkateswarlu, J. Chem. Phys. 47, 2334 (1967).

[7]J. H. Van Vleck, J. Chem. Phys. 7, 72 (1939).

[8]M. D. Sturge, in *Solid State Physics*, edited by F. Seitz, D. Turnbull, and H. Ehrenreich (Academic, New York, 1967), Vol. 20, p. 91.

[9]R. E. Peierls, *Quantum Theory of Solids* (Oxford U. P., London, 1965).

[10]M. C. M. O'Brien, J. Phys. C 5, 2045 (1972).

[11]F. S. Ham, Phys. Rev. 138, A1727 (1965).

[12]M. Caner and R. Englman, J. Chem. Phys. 44, 4054 (1966).

[13]J. Kanamori, Prog. Theor. Phys. 17, 177 (1957).

[14]M. D. Sturge, Phys. Rev. B 1, 1005 (1970).

[15]D. H. Goode, J. Chem. Phys. 43, 2830 (1965).

[16]D. T. Tearney, M. J. Freiser, and R. W. M. Stevenson, Phys. Rev. Lett. 9, 212 (1962).

[17]D. B. Eastman, Phys. Rev. 156, 645 (1967).

[18]A. L. Schawlow, A. M. Piksis, and S. Sugano, Phys. Rev. 122, 1409 (1961).

[19]F. S. Ham, Phys. Rev. 166, 307 (1968).

[20]J. Duran, Y. M. D'Aubigné, and R. Romestein, J. Phys. C 5, 2225 (1972).

[21]R. A. Cowley, Phys. Rev. 134, A981 (1964).

[22]T. Fujiwara, W. Gebhardt, K. Petanides, and Y. Tanabe, J. Phys. Soc. Jap. 33, 39 (1972).

[23]D. B. Fitchen, *Physics of Color Centers*, edited by W. Fowler (Academic, New York, 1968).

[24]C. M. Perry and E. F. Young, J. Appl. Phys. 38, 4616 (1967).

[25]K. V. Namjoshi, S. S. Mitra, and J. F. Veteline, Solid State Commun. 9, 185 (1971).

[26]E. F. Young and C. H. Perry, J. Appl. Phys. 38, 4624 (1967).

[27]I. Nakagawa, A. Tsuchida, and T. Shimanouchi, J. Chem. Phys. 47, 982 (1967).

[28]R. J. Elliott, M. F. Thorpe, G. F. Imbush, R. Loudon, and J. B. Parkinson, Phys. Rev. Lett. 21, 147 (1968).

[29]K. H. Huang and A. Rhys. Proc. R. Soc. A 204, 406 (1960).

[30]A. Tsuchida, J. Phys. Soc. Jap. 21, 2504 (1966).

[31]W. Moffitt and W. Thorson, Phys. Rev. 108, 1251 (1957).

[32]F. S. Ham, W. M. Schwarz, and M. C. M. O'Brien, Phys. Rev. 185, 548 (1969).

[33]M. D. Sturge and H. J. Guggenheim, Phys. Rev. B 4, 2092 (1971).

[34]M.-Y. Chen, thesis (University of Chicago, 1970) (unpublished); E. Solomon (unpublished).

[35]R. L. Melcher and D. J. Bolef, Phys. Rev. 178, 864 (1969).